Combining computational fluid dynamics and neural networks to characterize microclimate extremes: Learning the complex interactions

Science of the Total Environment 829 (2022) 154223

Contents lists available at ScienceDirect

Science of the Total Environment

journal homepage: www.elsevier.com/locate/scitotenv

Combining computational fluid dynamics and neural networks to characterize microclimate extremes: Learning the complex interactions between meso-climate and urban morphology

Kavan Javanroodi [a,*], Vahid M. Nik [b,c], Marco G. Giometto [d], Jean-Louis Scartezzini [a]

[a] Solar Energy and Building Physics Laboratory, Ecole Polytechnique Fédérale de Lausanne, Switzerland
[b] Division of Building Physics, Department of Building and Environmental Technology, Lund University, Sweden
[c] Division of Building Technology, Department of Architecture and Civil Engineering, Chalmers University of Technology, Sweden
[d] Department of Civil Engineering and Engineering Mechanics, Columbia University, United States of America

HIGHLIGHTS

- A data-driven model to downscale weather extremes using CFD and Neural-Networks
- Numerical simulations are validated against high-resolution in-situ measurements.
- A novel urban canopy parameterization method developed to model urban morphologies
- The model probed reliable in predicting extreme microclimate conditions.
- The model can be readily used in urban-energy and -comfort studies.

GRAPHICAL ABSTRACT

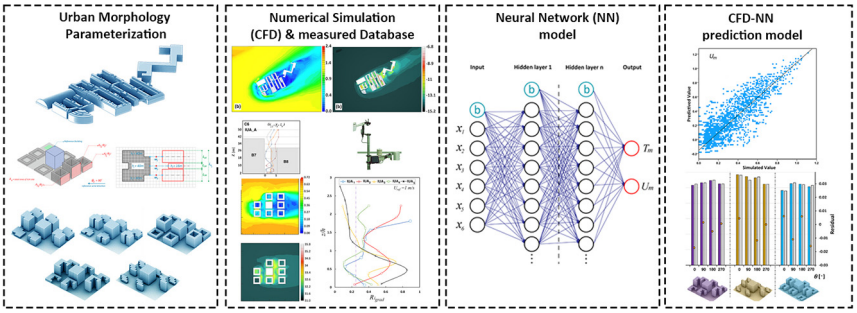

ARTICLE INFO

Article history:
Received 24 October 2021
Received in revised form 2 February 2022
Accepted 25 February 2022
Available online 1 March 2022

Editor: Scott Sheridan

Keywords:
Extreme microclimate conditions
Urban morphology
CFD simulations
Neural networks

ABSTRACT

The urban form and extreme microclimate events can have an important impact on the energy performance of buildings, urban comfort and human health. State-of-the-art building energy simulations require information on the urban microclimate, but typically rely on ad-hoc numerical simulations, expensive in-situ measurements, or data from nearby weather stations. As such, they do not account for the full range of possible urban microclimate variability and findings cannot be generalized across urban morphologies. To bridge this knowledge gap, this study proposes two data-driven models to downscale climate variables from the meso to the micro scale in arbitrary urban morphologies, with a focus on extreme climate conditions. The models are based on a feedforward and a deep neural network (NN) architecture, and are trained using results from computational fluid dynamics (CFD) simulations of flow over a series of idealized but representative urban environments, spanning a realistic range of urban morphologies. Both models feature a relatively good agreement with corresponding CFD training data, with a coefficient of determination $R^2 = 0.91$ ($R^2 = 0.89$) and $R^2 = 0.94$ ($R^2 = 0.92$) for spatially-distributed wind magnitude and air temperature for the deep NN (feedforward NN). The models generalize well for unseen urban morphologies and mesoscale input data that are

Abbreviations: ABL, Atmospheric Boundary Layer; ADAM, Adaptive Moment Estimation; AEV, algebraic eddy-viscosity model; BMC, Building Modular Cell; CFD, computational fluid dynamics; DNN, Deep Neural Network; ECD, Extreme Cold Day; EWD, Extreme Warm Day; FEM, Finite Element Method; GDM, Gradient Descent with Momentum; H/W, canyon height to width ratio; Hn, Normalized Height; IUA, Idealized Urban Areas; L/H, Canyon Length to Height ratio; Le, Effective Length; MLP, Multilayer Perceptron; NN, Neural Networks; PAR, Plot Area Ratio; RANS, Reynolds-averaged Navier–Stokes; RL, Roughness Length; RMSE, Root Mean Square Error; RSL, roughness sub-layer; SCI, Site Coverage Index; SVF, Sky View Factor; TDD, Typical Temperature Day; TKE, Turbulence Kinetic Energy; TMY, Typical Meteorological Year; UCL, urban canopy layer; UHI, urban heat island; VAR, Volume Area Ratio.

* Corresponding author.
E-mail addresses: kavan.javanroodi@epfl.ch (K. Javanroodi), vahid.nik@byggtek.lth.se vahid.nik@chalmers.se (V.M. Nik), mg3929@columbia.edu (M.G. Giometto), jean-louis.scartezzini@epfl.ch (J.-L. Scartezzini).

http://dx.doi.org/10.1016/j.scitotenv.2022.154223

Wind speed
Air temperature

within the training bounds in the parameter space, with a $R^2 = 0.74$ ($R^2 = 0.69$) and $R^2 = 0.81$ ($R^2 = 0.74$) for wind magnitude and air temperature for the deep NN (feedforward NN). The accuracy and efficiency of the proposed CFD-NN models makes them well suited for the design of climate-resilient buildings at the early design stage.

1. Introduction

According to a recent report from the World Health Organization, over 74% of the European population and 55% of the world's population live in urban areas (Brockerhoff and Nations U, 2018). These numbers will increase by 2050, accelerating the urbanization rates and consequently increasing the number of megacities (i.e. urban areas with more than one million citizens) from 512 in 2016 to 662 in 2030 (World Urbanization Prospects, 2018). The massive construction wave that persisted throughout the last century in response to ever-increasing housing demands (Bhatta, 2010) has introduced new challenges in cities and exacerbated existing ones, including shortage of housing, lack of civil infrastructure, increased air pollution, and high peak energy demands, among others. These challenges are particularly present in suburban areas just outside big cities (IVA, 2017). As a result, several interconnected urban areas have emerged with different morphological characteristics, such as different land cover patterns and urban forms. These characteristics affect the urban microclimate, which depend on the spatial arrangement of buildings, their geometry, material, geographical siting, and human activities (Oke, 2017). The urban microclimate affects the outdoor comfort (Peng et al., 2019) and health (Schinasi et al., 2018) of urban dwellers, as well as the performance of buildings and associated engineering applications (Hosseini et al., 2022; Castaldo et al., 2018). To a lesser degree, they also affect the air quality in indoor spaces and their thermal comfort (Taleghani et al., 2019).

It is well known that cities are usually warmer and characterized by lower wind speeds than their surrounding rural areas (Oke, 1987). However, the geometry of cities is intrinsically heterogeneous, and local microclimates can vary significantly over a broad range of spatiotemporal scales (Javanroodi and Nik, 2020). For example, microscale variations of the wind speed in the urban canopy layer — which extends from the ground up to the mean height of the canopy — can affect the local ventilation (Hsieh and Huang, 2016), lead to local accumulation of airborne pollutions (Yang et al., 2020), or yield high wind speed magnitudes that negatively affect pedestrian comfort (Tsichritzis and Nikolopoulou, 2019). Conditions are expected to worsen because of climate change, which will lead to more significant and more frequent extreme climatic events (Yang et al., 2022; Perera et al., 2021a). Climate change and extreme events can considerably affect the energy performance of buildings as well as the comfort and wellbeing of urban dwellers, especially in large urban agglomerations (L. Lin et al., 2020; Yang et al., 2021). This can challenge energy sustainability and security in urban areas. To develop sound urban climate adaptation strategies, it is hence crucial to predict extreme urban microclimate events. Predictive models should be based on methodologies that accurately capture the non-linear interaction between climate variables and urban morphologies.

The existing research efforts in mapping urban morphology to urban microclimate can be broadly divided into two main groups: the first devoted to elucidating the physics underpinning the interaction between urban morphology and climate variables (a.k.a., Urban Physics (Blocken, 2015)); and the second focusing on the development of predictive models for climate variable — wind speed, air temperature, and humidity — for energy calculations or urban sustainability applications (Javanroodi et al., 2018). The common morphological parameters adopted in these studies relate to the horizontal and vertical density of urban areas (Garuma, 2018; Chokhachian et al., 2020). Parameters such as building coverage ratio (BCR) (Mortezazadeh et al., 2021), planar area fraction (λ_p) (C. Yuan et al., 2020), building height (BH) and frontal area index (FAI or λ_f) (Apreda et al., 2020), building volume density (BVD) (Cao et al., 2021), and canyon aspect ratio (H/W) (Liu et al., 2020) have been widely used to highlight interdependencies between urban form and urban microclimate. Additional parameters include the sky view factor (SVF) (Dirksen et al., 2019), the sky exposure factor (SEF) (Yi and Kim, 2017), and the surface drag coefficient (C_d) (Mo et al., 2021). Research studies focusing on urban physics typically develop models that map a combination of these input parameters to quantities of interest such as urban temperature (Jamei et al., 2017), wind speed (Kikumoto et al., 2018; Javanroodi et al., 2021), and solar radiation (Zhang et al., 2019).

Thanks to advances in computing hardware and software, computational fluid dynamics (*CFD*) is rapidly establishing itself as the go-to approach for microclimate studies (Toparlar et al., 2017). Most CFD studies on microclimate and urban form are focused on assessing air temperature and wind characteristics (Y. Lin et al., 2020). Li et al. (2019) and Giridharan and Emmanuel (2018) provided extensive reviews on temperature and urban heat island (UHI), while Toja-Silva et al. (2018) and Mittal et al. (2018) reviewed the works on urban morphology parameters and wind flow characteristics. Allegrini et al. (2014) showed that higher surface temperatures can induce buoyancy-driven flows in the UCL under weak wind conditions, with associated enhancement of the local turbulent kinetic energy (Allegrini, 2018), lower air temperature, and higher wind speeds inside and above UCL was reported for urban areas with non-uniform building heights when compared to corresponding urban environments with uniform building height. Thermal circulations can also contribute to heat removal in street canyons (Nardecchia et al., 2016). This condition, in some cases, may decrease surface temperature (Chen et al., 2020) or may increase pedestrian thermal comfort in the canopies with a larger canyon height to width ratio (Zhang et al., 2017). Higher wind speeds in colder climates can increase urban discomfort due to the high wind chill factor by reducing the sensible temperature at the pedestrian level (Lin et al., 2019). High wind speeds in the UCL can also result in higher heating demands in wintertime due to air infiltration through building envelopes (Guillén-Lambea et al., 2019), whereas low wind speeds in the UCL can reduce the natural ventilation potential in summer (Wang et al., 2018).

These contrasting effects highlight some of the challenges associated with the design of balanced urban environments. Despite decades of active research, most existing studies leveraging CFD have typically focused on a limited number of climate variables, and either considered very idealized setups (Giometto et al., 2016; Wang et al., 2016; Kalogirou, 2001; Marugán et al., 2018; Zendehboudi et al., 2018; Becker and Thrän, 2017) or very specific realistic urban morphologies (Giometto et al., 2016). Findings from idealized simulations such as flow over cuboid arrays might be difficult to generalize to realistic urban environments, whereas case studies are in general highly site-specific. On the other hand, studies relying on experimental measurements typically rely on sparse in-situ points measurements of climate variables, whose representativeness for the neighborhood- or city-averaged quantities is questionable due to the intrinsic heterogeneity of urban microclimate conditions (Giometto et al., 2016). The wide range of spatiotemporal scales characterizing urban microclimate processes and their inherently chaotic nature represents the main challenge associated with the development of a universal urban canopy parameterization.

In part motivated by the aforementioned challenges, the recent decades have seen a rising trend in the deployment of data-driven models to address problems pertaining to the field of urban and building physics. With the rapid development of computing power and higher data availability, developing hybrid frameworks that combine physics-based and data-driven approaches is becoming increasingly popular among researchers. Several Machine Learning (ML) techniques have proven robust, reliable, and efficient in dealing with sparse and multivariate climate datasets (Wang et al., 2016). ML techniques have been widely adopted to predict renewable

energy resources in urban areas (Kalogirou, 2001). For example, Marugán et al. (2018) conducted an extensive review on the use of Neural Networks (NN) models for wind energy systems, with a lens on their capabilities for predicting wind power. Zendehboudi et al. (2018) reviewed the current state of the art in predicting wind and solar energy potentials in urban areas using Support Vector Machines models. Other ML techniques such as Random Forests (Becker and Thrän, 2017) and Bayesian inference (Sousa and Gorlé, 2019) have also been used to predict wind power and urban flow characteristics.

Lately, NN models have received increasing attention from the urban climate and building energy communities (Ferrero Bermejo et al., 2019; Mi and Zhao, 2020). A high number of studies adopted NN to predict the energy performance of buildings in urban areas (Abbasabadi and Ashayeri, 2019; Mohandes et al., 2019; Roman et al., 2020). NN models have also been leveraged to predict air and surface temperature (Papantoniou and Kolokotsa, 2016), the UHI effect (Asadi et al., 2020), wind speed in the UCL (Mauree et al., 2019), and relative humidity (Mba et al., 2016) in microscale models driven by historical mesoscale or in-situ measured weather. The most widely used NN models in these studies pertain to the supervised learning category and are conventional feedforward networks such as Multilayer Perceptron (MLP) or more sophisticated class neural networks such as Recurrent Neural Networks (RNN). Some studies (M.-D. Liu et al., 2021; X. Liu et al., 2021; Han et al., 2021) highlighted the superior performance of RNN models compared to alternative formulations for processing time-series data, thanks to their memory awareness (Hochreiter and Schmidhuber, 1997). However, RNNs are computationally expensive and require extensive datasets with high temporal resolutions to enable short- and mid-term predictions. Because of this, feedforward networks are usually the preferred approach to efficiently predict average daily or annual climate variables based on scarce datasets with low temporal resolutions and high generalization capability (Mocanu et al., 2018). Deep Neural Networks (DNN) is a class of ANN models with multiple hidden layers, which are capable of capturing complex non-linearities such as those characterizing weather forecasting models (Hu et al., 2016). The DNN-based models have proved able to achieve higher levels of accuracy and generalization for the prediction of short-, mid-, and long-term renewable energy resources (wind, solar) when compared to shallow networks (Zhou et al., 2021; Aslam et al., 2021) and solar energy (Alkhayat and Mehmood, 2021). Q. Yuan et al. (2020) conducted an extensive review on the application of DNN models in predicting air temperature based on morphological parameters (e.g., land cover, vegetation parameter, etc.) using environmental remote sensing data.

A major challenge in the use of data-driven models to predict spatiotemporal variations in microclimate conditions in the UCL is represented by their need for spatially-distributed meteorological data encompassing a representative range of urban microclimate conditions, which are not readily available. Long-term in-situ measurement campaigns in urban environments are scarce, mainly because of the high costs of deploying instruments in urban areas and difficulties associated with obtaining permits, and they are also typically limited to point wise information, which might

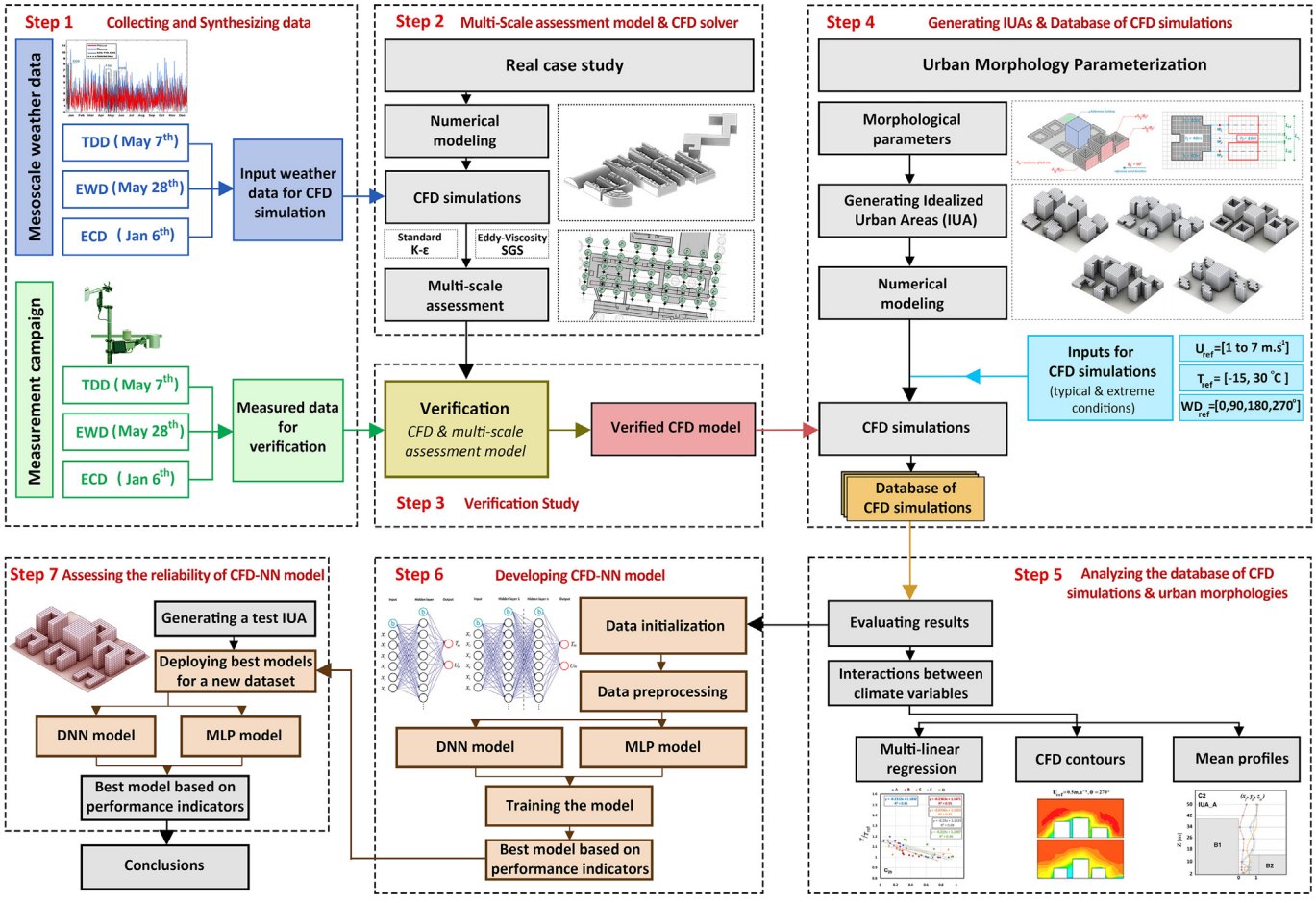

Fig. 1. Schematic workflow of the study: Step 1: collecting and synthesizing mesoscale and in-situ measured weather data; Step 2: developing multi-scale assessment model and CFD solver for the real case study using Standard k-ε model and AEV turbulence models; Step 3: verifying the multi-scale assessment model and CFD solver against in-situ measured data; Step 4: developing urban morphology parameterization method and five idealized urban morphologies to generate the database of CFD simulations; Step 5: evaluating the database of CFD simulation based on morphological parameters; Step 6: developing CFD-NN model based on two architectures (DNN, and MLP); Step 7: employing the best performance CFD-NN model for a new set of morphological data.

not be representative of corresponding area-averaged quantities in the UCL (Wang and Wu, 2016). CFD simulations offer an opportunity to in part bridge this knowledge gap, thanks to their capability to efficiently generate a large amount of spatially distributed microclimate data. To date, only a few studies have used CFD simulations to train NNs for the prediction of microclimate variables, but mostly focusing on natural terrain environments (Marquez et al., 2013; Yi and Malkawi, 2011).

To overcome issues related to the scarcity of comprehensive microclimate measurements in urban areas, we propose a framework using two NN models that uses CFD results to downscale climate variables from the mesoscale to the microscale in arbitrary urban geometries. The NN models are trained on a database of CFD-generated urban microclimates with varying morphologies to predict spatially-distributed and time-averaged wind speed and air temperature magnitudes in the UCL (Fig. 1). The CFD model is developed and validated against in-situ measurements in a selected urban area for typical and two extreme weather conditions (Steps 1 to 3). The validated CFD model is then used to inform the development of parameterized idealized urban environments, over which we conduct an extensive series of CFD simulations, considering both typical and extreme climate conditions (Steps 4 and 5). Next, the database of CFD simulations is fed into two NN predictive models using MLP and DNN architectures which take morphological parameters and mesoscale weather data as inputs (Step 6). Finally, the developed models are deployed to predict wind speed and air temperature variations for a new urban area to examine their capability to extrapolate to unseen environments (Step 7).

This manuscript is organized as follows. Section 2 presents the selected case study, details of the measurement campaign, and the mesoscale weather data. It also provides an overview of numerical simulations as well as of the multi-scale microclimate assessment approach. The performance of the assessment approach is then verified in Section 3, across the considered climate conditions. The urban morphology parameterization method and developed idealized urban areas are described in Section 4. The hybrid CFD-NN model is discussed in Section 5. The Result and Discussion section (Section 6) first assesses the interactions between climate variables and urban morphologies (Section 6.1), and the performance of the CFD-NN models are evaluated in Section 6.2, and the reliability of the developed models for a new set of morphological data is analyzed in Section 6.3. Limitations of the study are discussed in Section 6.4 and concluding remarks are provided in Section 7.

2. Developing a microclimate assessment model

2.1. Study area and measurement campaign

Stockholm City is located on fifteen islands on the east coast of Sweden, with eleven municipal districts and over 118 km^2 of total area. It is the most populated city in Sweden with several interconnected complex geometric urban forms, ranging from dense city centers to detached buildings (Nielsen, 2015). The city is experiencing an exceptionally high rate of expansion and boom in construction to accommodate the rapid growth of its population, especially in the districts located at the border line of the city enclosure (Sweden's National Report for the third United Nations Conference on Housing and Sustainable Urban Development (Habitat III). Swedish National Report, n.d.). The considered study area is called Norra

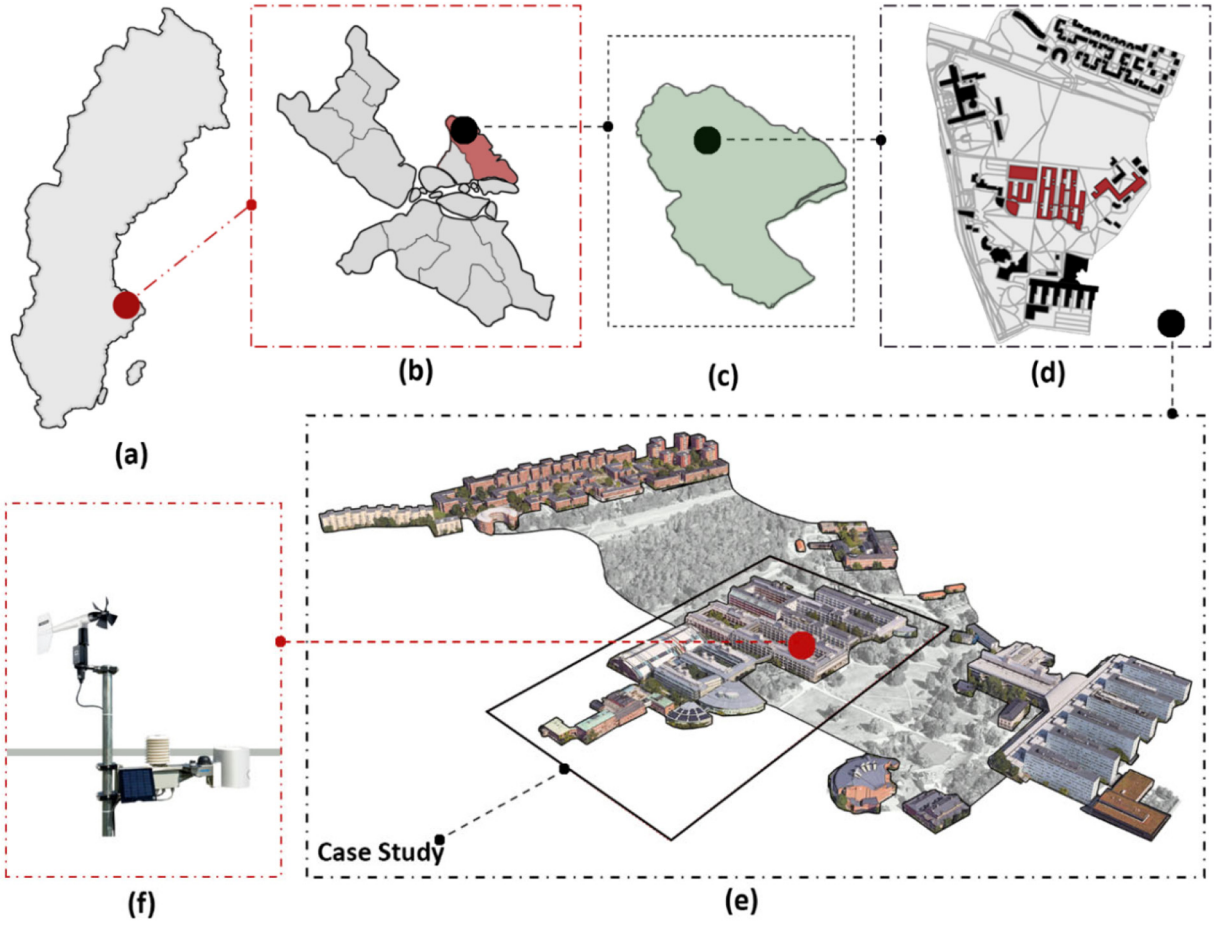

Fig. 2. Schematic and rendering of the study area: (a) Sweden, (b) Stockholm, Östermalm (c) Norra Djurgårdsstaden, (d) Stockholm University, Frescati Campus and the selected case study, (f and e) Mounted weather station on the roof top of Arrhenius Laboratory building, Pessl iMETOS located at 59°21′56.3″N and 18°03′34.2″E, 26 m higher than the ground surface.

Djurgårdsstaden, located in the Östermalm district. The district hosts 73.5 thousand inhabitants (2016), which is expected to increase to above 104 thousand by 2040 through transforming from an old seaport to a combination of new constructions within a vast natural environment (Fig. 2) (City Planning Administration, 2018). A microclimate measurement campaign has been conducted in this area to evaluate the impact of urban morphology on the local microclimate conditions. One year of continuous measurements, from 00:00, January 1st to 23:00, December 31st, 2018, was carried out with hourly temporal resolution leveraging a Pessl iMETOS Weather Station (sampling frequency of 10 min) mounted on the roof of the Arrhenius Laboratory on Frescati Campus, Department of Meteorology (MISU), Stockholm University (Weather Station - Department of Meteorology, n.d.). The weather station is located at 59°21′56.3″N and 18°03′34.2″E, and is 26 m tall. This station uses a RM YOUNG wind monitor for measuring wind speeds (accuracy: ±0.3 m/s) and directions (accuracy: ±3°); and a HygroClip sensor for measuring temperature, relative humidity, and dew point. In an effort to reduce the computational cost of CFD simulations while accounting for the impact of surrounding obstacles on the measured data, all major buildings and obstacles taller than 3 m within a 230m radius from the weather station were modeled and ingested into the CFD solver.

2.2. Mesoscale weather dataset

Stockholm has an oceanic climate with high humidity and over 47% annual wet days (Beck et al., 2018). The recorded long-term (1981 and 2016) average daytime temperature in Stockholm is −1 to 4 °C in winter and 20 to 25 °C in summer. In terms of extremes, the temperature occasionally drops below −15°C in winter and rarely rises over 30 °C in summer. The average daily wind speed is 3.5 m/s in winter and around 2.6 m/s in summer (Sweden Weather|SMHI, n.d.). The variations of wind speed are high and depend on several factors such as the local topography and temperature variations. Fig. 3(a, b) compares the Typical Meteorological Year (TMY) temperature and wind speed (the so-called mesoscale data) against measured data at the study area. This study adopted a method developed by Nik (2016) to synthesize typical and extreme weather files based on the outdoor temperature. The method selects representative and extreme months based on the Finkelstein–Schafer statistics. In this study, a similar logic is applied on the weekly scale, whereby weekly mean air temperature is used as the indicator to synthesize meteorological days with typical, extreme high, and extreme low temperature (for more details about the method and adopted procedures, the readers are referred to the previous works by the authors (Javanroodi and Nik, 2019, 2020)). Three 24-hour weather data are considered as input for conducting the validation study, including the most typical, warmest and coldest days: Typical Temperature Day (TTD), Extreme Warm Day (EWD), and Extreme Cold Day (ECD). The corresponding hourly climate variables for each of these three days are then used as reference weather data inputs to guide the CFD simulations. The considered climate variables are wind speed, wind direction, air temperature, global horizontal irradiance, relative humidity, and cloud coverage. Wind direction (WD) with an hourly resolution for these three cases is depicted in Fig. 3(c).

2.3. Setup of the CFD solver

Numerical simulations are conducted via a 3D Reynolds-average Navier-Stokes (RANS) CFD solver. RANS models present an optimal compromise between accuracy and efficiency for building- and terrain-resolving microclimate studies (Oke, 1987). Alternative approaches such

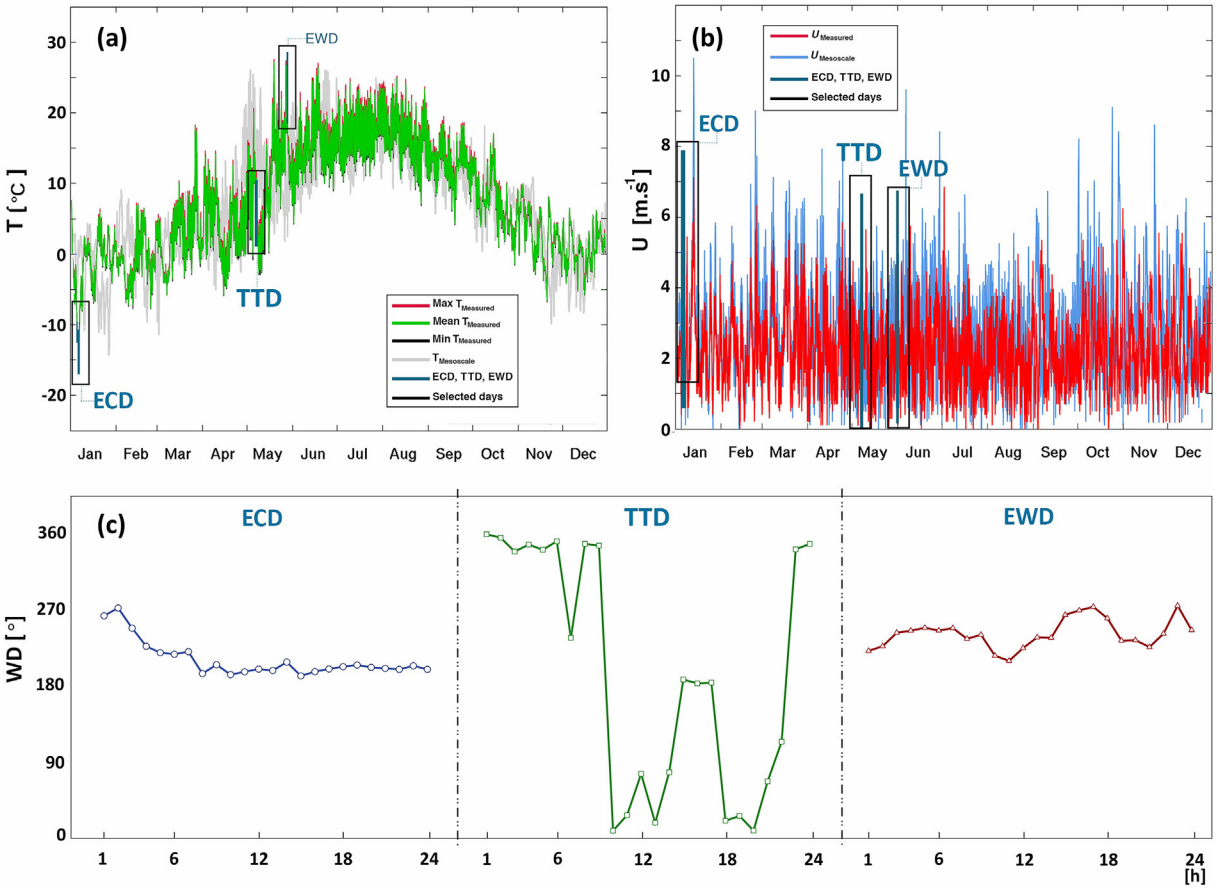

Fig. 3. Weather conditions and selected typical and extreme days in the studied area, including ECD (January 6th), TTD (May 7th), EWD (May 28th). (a): maximum, mean, and minimum measured temperature vs TMY, (b): measured wind speed vs TMY, (c) *hourly wind directions.*

as those based on the Large Eddy Simulation (LES) technique provide enhanced accuracy, especially in the UCL and regions of massive flow separation, but are significantly more expensive from a computational perspective and require dedicated high-performance computing resources (Lenz et al., 2019). In this study, two RANS closure models are considered: A two-equation turbulence model (Standard k-ε model) and a zero-equation turbulence model (algebraic eddy-viscosity model). The performances of these models are assessed against in-situ measurements. We solve the ensemble-averaged continuity, momentum, temperature and moisture conservation equations, under the Boussinesq approximation for the evaluation of buoyancy terms (Schnipke, 1986). The k-ε model relies on the Boussinesq approximation to evaluate μ_t (eddy viscosity) and k_t (eddy diffusivity) using Eqs. (1) and (2):

$$\mu_t = \rho C_\mu \frac{K^2}{\varepsilon} \tag{1}$$

$$k_t = \frac{\mu_t C_p}{Pr_t} \tag{2}$$

where ρ is a constant density, K is the turbulent kinetic energy, ε is the rate of kinetic energy dissipation, adn Pr_t is the turbulent Prandtl number. In the Standard k-ε model, Reynolds stresses ($\rho\overline{u_i u_j}$) are parameterized as a function of the turbulent kinetic energy (K) and turbulent energy dissipation (ε), whose evolution is described via Eqs. (3) and (4), respectively:

$$\frac{\partial(\rho K)}{\partial t} + \frac{\partial(\rho K u_i)}{\partial x_i} = \frac{\partial}{\partial x_i}\cdot\left(\frac{\mu_t}{\sigma_k}\frac{\partial K}{\partial x_i}\right) - \rho\varepsilon + 2\mu_t \cdot S_{ij}\cdot S_{ij} \tag{3}$$

$$\frac{\partial(\rho\varepsilon)}{\partial t} + \frac{\partial(\rho\varepsilon u_i)}{\partial x_i} = \frac{\partial}{\partial x_i}\cdot\left(\frac{\mu_t}{\sigma_\varepsilon}\frac{\partial \varepsilon}{\partial x_i}\right) + C_{1\varepsilon}\frac{\varepsilon}{K}2\mu_t S_{ij}\cdot S_{ij} - C_{2\varepsilon}\rho\frac{\varepsilon^2}{K} \tag{4}$$

($\sigma_k = 1$, $\sigma_\varepsilon = 1.30$, $C_{1\varepsilon} = 1.44$, $C_{2\varepsilon} = 1.92$, $C_\mu = 0.09$)

The turbulent kinetic energy at the inflow is prescribed via Eq. (5),

$$K = 0.5\left[(Iu)^2 + (Iv)^2 + (Iw)^2\right] \tag{5}$$

where $I = \frac{u'}{u} = \frac{v'}{v} = \frac{w'}{w}$ is the turbulence intensity and u, v and w are the ensemble time-averaged mean velocity (u', v', *and* w' *are* velocity fluctuations). The ensemble-averaged strain rate tensor, S_{ij} is defined via Eq. (6):

$$S_{ij} = \frac{1}{2}\left(\frac{\partial u_i}{\partial x_i} + \frac{\partial u_j}{\partial x_i}\right) \tag{6}$$

here u_i is is the velocity vector, and x_j is the independent coordinate.

An algebraic eddy-viscosity model (AEV) is also considered, which is less accurate and generalizable when compared to the k-ε model, but more efficient. Studies showed that the algebraic eddy-viscosity model can yield an acceptable performance depending on the scope of the study (Bazargan and Mohseni, 2012). An algebraic equilibrium wall-layer model is adopted to model Reynolds stresses and turbulent heat fluxes at the building facets and street surfaces. The wall layer model is based on Eq. (7):

$$U^+ = \kappa^{-1}\, log\, y^+ + B - \kappa^{-1}\, log\left(1 + .3\frac{rS_V}{v}\right) \tag{7}$$

where v is the kinematic viscosity, S_V is shear velocity, and r ($r = 0.017$ m (Ricci et al., 2020)) is the equivalent sand-grain roughness height, $B = 5.5$ and $\kappa = 0.4$ are a dimensionless parameter and the von-Kármán constant. The turbulent heat transfer is enforced based on Spalding's Inner Law (Mandal and Mazumdar, 2015), depending on values of turbulent and laminar Prandtl numbers. The Turbulent Prandtl number is evaluated via Eq. (8):

$$P_r = \frac{C_p \mu}{k} \tag{8}$$

where, k and μ are thermal conductivity and dynamic viscosity of the fluid, and C_p is the specific heat coefficient of the fluid (constant volume). Air is treated as a homogenous mixture, with density given by Eq. (9)

$$\rho = (1 - f)\rho_a + f\rho_m \tag{9}$$

Here, ρ_a and ρ_m are air density and moist air density respectively, and f is mixture fraction condensed water. The mixture fraction and humidity are calculated at each node in the computational domain using an additional partial differential equation. Moreover, a radiation model is used to calculate solar heating through radiative heat transfer based on the True View Factor and solar heating energy balance equation (CFD, 2019). In this regard, an additional heat flux term (q_{ri}) is assigned to the wall elements to calculate surface-to-surface radiant exchange given by Eq. (10).

$$q_{ri} = A_i(G_i - J_i) \tag{10}$$

here, A_i is the wall of element i surface, G_i and J_i are respectively incmoing radiation and radiosity of element i calculated from Eqs. (11) and (12):

$$J_i = (1 - \varepsilon_i - \tau_i)G_i + \varepsilon_i E_{bi} \tag{11}$$

$$G_i = \sum_{j-1}^{N} J_j F_{i-j} \tag{12}$$

where τ_i and ε_i are transmissivity and emissivity, and E_{bi} is black body emissive power of element i. The calculation of black body emissive power is based on Stefan-Boltzmann constant (5.669×10^{-8} W/m^2-K^4) and the surface temperature of element i. The view factor ($F_{i\text{-}j}$), is calculated by projecting an image of the element faces on the sky dome (to compute the shadowing effects), considering the reciprocity of factors ($F_{ij} = F_{ji}$). Adopting view factors as inputs, the solar heat flux is calculated for each element based on geospatial coordinate (Stockholm), as well as the date, and time of the simulation.

Fig. A.1-a in Appendix A illustrates the defined computational domain and boundary conditions based on standards like AIJ and COST guidelines (Mochida et al., 2002; Tominaga et al., 2008). The vertical and lateral extent of computational domain are 10H and 20H respectively (H is 26 m for the selected case and 48 m for the IUAs). Symmetry boundary conditions are imposed on the lateral surfaces of the domain. Wind speed, air temperature, and humidity boundary conditions are defined at the inlet, while the outlet is set to a uniform zero gradient conditions. The ground surface is assigned an albedo of 0.5 (asphalt). The model is discretized based on stabilized Finite Element Method (FEM), where advection terms are discretized based on a modified streamline upwind method in the solver and the SIMPLE-R (Semi-Implicit Method for Pressure Linked Equations-Revised) technique is used for the velocity-pressure coupling (CFD, 2019; Patankar, 1980). Each idealized urban model in this study has about 620000 hexahedral elements (mesh resolutions of 0.3 m). Convergences are monitored at multiple defined monitor points throughout the computational domain and a tolerance of 10^{-4} for the Turbulence Kinetic Energy (TKE) and continuity terms and 10^{-6} for all other terms is considered. We found such values to be sufficient to yield converged solutions by programmatically varying tolerances for a reference case. Simulations are conducted using Autodesk CFD. The CFD solver has also been previously validated by the authors (Javanroodi et al., 2018; Javanroodi and Nik, 2020) under a similar problem setup (against wind tunnel data, ANSYS Fluent simulations, and Silsoe cube (Richards et al., 2001)).

2.4. Multi-scale microclimate assessment approach

Fig. 4-a depicts a portion of the urban boundary layer for the considered study area. We validate the model against the in-situ measurements while at the same time also characterizing CFD model predictions across a range of scales within the urban roughness sublayer (RSL)—defined as that layer of the atmosphere that extends from the ground up to 5 times

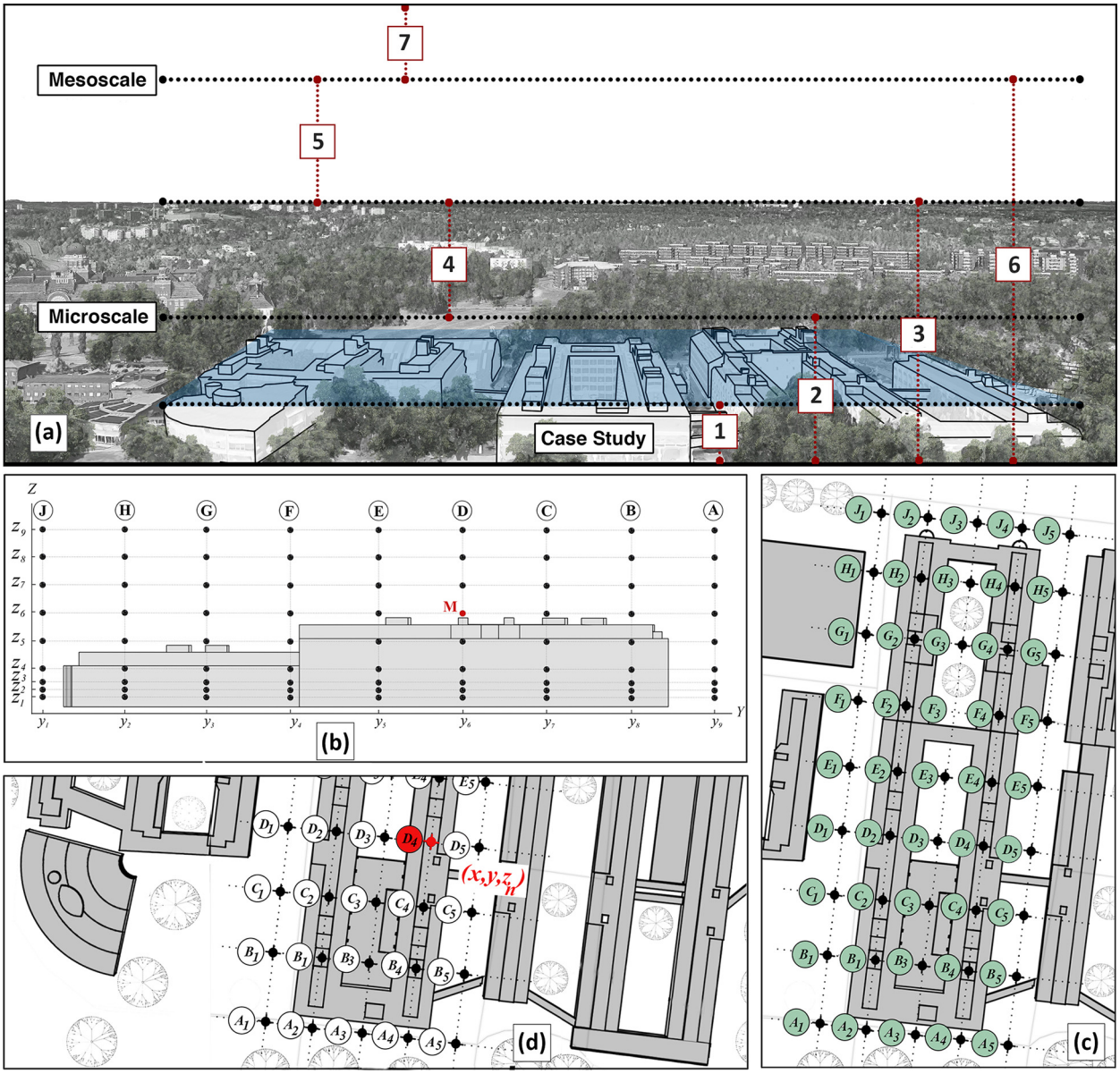

Fig. 4. (a): The definition of microscale and mesoscale based on Oke (Oke, 1987): 1) Urban canopy layer, 2) Roughness sub-layer, 3) Surface layer, 4) Inertial sub-layer, 5) Mixed layer, 6) Urban boundary layer, 7) Free atmosphere; (b): Nine vertical layers over which monitor points are defined. (c): First scenario (S_1): 341 monitor points, (d): Second scenario (S2): one monitor point at 26 m height sited at the location of the weather station.

the mean building height (Oke, 2017). Specifically, we define two spatial averaging scenarios, based on a set of "monitor" points in space. A total of 341 monitor points are defined over and within the urban surface, organized into a 9 × 5 grid of constant 16 m stencil over the horizontal plane, and nine vertical layers spanning from 2 m to 50 m above ground level. In the first scenario, S_1 (Fig. 4-c), wind velocities and air temperature are averaged over the 341 monitor points; in the second scenario, S_2 (Fig. 4-d), only one monitor point at the location of the in-situ measurement is considered. CFD results for each of the considered scenarios and flow statistic are compared against corresponding in-situ measurements.

3. CFD model validation

In this section, we compare predictions from the k-ε and AEV models against time-varying wind speed, air temperature, and humidity from the in-situ measurements for the two aforementioned averaging scenarios. Twenty-four CFD simulations were conducted for each of the ECD, TTD, and EWD cases (seventy-two simulations in total), forcing the CFD model via the mesoscale wind speed (U_{ref}), wind direction (θ_{ref}), air temperature (T_{ref}), and relative humidity (RH_{ref}) variables. Fig. 5 compares microscale, measured, and mesoscale wind speed and temperature for ECD (January 6th, 2018), TTD (May 7th, 2018) and EWD (May 28th, 2018). An overview of the wind speed results shows a good agreement between simulated data and measured data using the Standard k-ε model at the measurement location (S3), while the AEV model overpredicts the measurements. These results are in line with findings from previous studies such as Moonen et al. (2012), and Ricci et al. (2020). For S_2 and S_1 scenarios (Section 2.4); the average wind speed and standard deviation using k-ε model have less than 8% relative difference compared to measured data. These differences are up to 31% and 39% for wind speed and its standard deviation using the AEV turbulence model.

In terms of air temperature at the microscale, predictions from the Standard k-ε model are in good agreement with measured data for the S_1

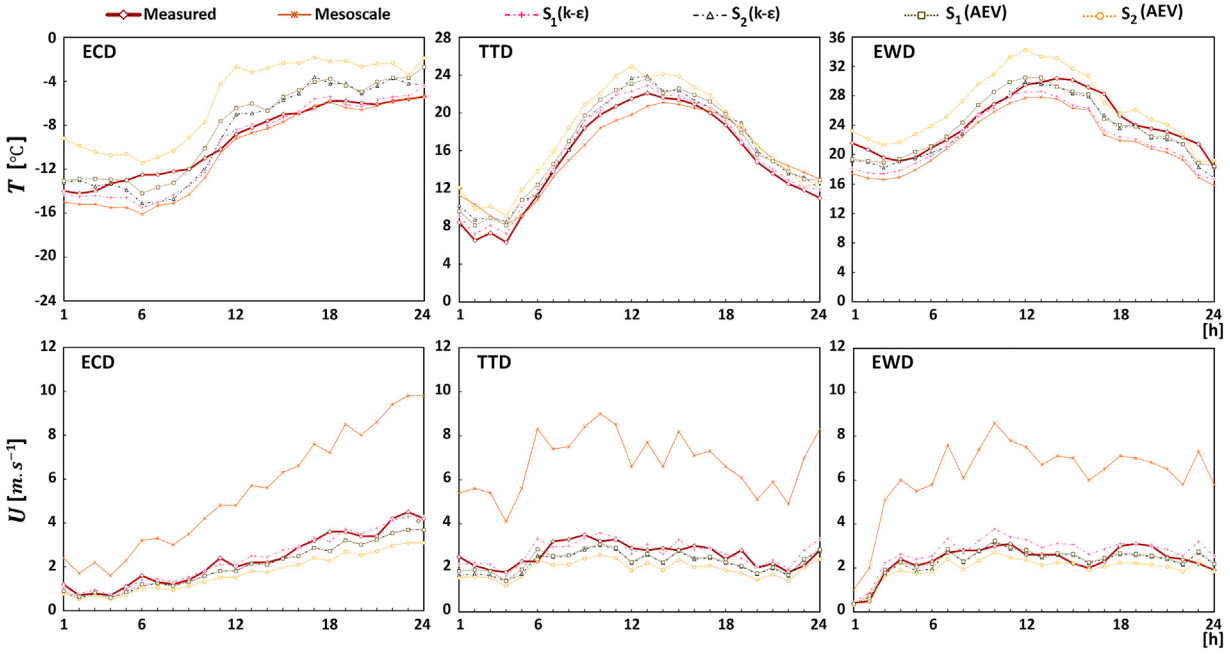

Fig. 5. Comparison between mesoscale, measured, and microscale CFD temperature and wind speed magnitudes across the considered real urban area based on convergence scenarios (S_1, S_2). Left panel: ECD; Mid panel: TTD; Right panel: EWD.

scenario during all of the considered days, while the AEV model overestimates temperatures throughout. For example, in ECD, the difference between the measured and simulated temperature at S_2, and S_1 are 13%, and 7% for the Standard k-ε model, and 14%, and 21% for AEV model. In EWY, the temperature difference between CFD simulation using k-ε model and measured data was higher (up to 1.5 °C for S_1) when compared to the ECD and TTD conditions. This behavior can be related to the presence of a UHI, which the CFD model fails to capture. The AEV model is five times more efficient than the two equations model, but it failed to estimate wind speed and air temperature properly for all the considered days. Thus, considering its higher accuracy and reasonable computational load, the Standard k-ε model and S_1 convergence scenario is adopted in the CFD solver for the idealized urban areas (See Fig. A.2 in Appendix A comparing plan-view CFD contours at 2 m height from surface ground for wind velocity and air temperature using Standard k-ε and AEV turbulence models).

4. Development of an urban morphology parameterization method

4.1. Definition of morphological parameters

As discussed in the literature review, several morphological parameters have been adopted to assess the microclimate conditions. In this study, eight well-established morphological parameters that are commonly adopted in the building energy community are used to develop the urban morphology parameterization method (Fig. 6). The main parameter used to quantify the horizontal expansion in this study is Plot Area Ratio (*PAR*). This parameter is the total floor area of the buildings divided by the total site area, and is defined via Eq. (13):

$$PAR = \frac{\left(\sum_{i=1} A_i\right) \times m_i}{A_a} \tag{13}$$

where, A_i is the floor area of the building *i* multiplied by its number of floors (*m*), and A_a is the total horizontal area of the site. To parametrize the characteristic of each building as a function of its sub-site (for each building), Site Coverage Index (*SCI*) is developed as the total area of the ground floor of buildings (A_g) divided by the total area of the sub-site (A_s) using Eq. (14):

$$SCI = \sum_{i=1}^{n} \left(A_{g_i} \cdot A_s{}^{-1}\right) \tag{14}$$

To account for height-related information, two other parameters are here introduced, namely the Volume Area Ratio (*VAR*) and the Frontal Area Density (λ_f) given by Eqs. (15) and (16) respectively. *VAR* is calculated based on the total volume of buildings ($A.h$) divided by the site area (A_a) and mean height of urban area (z_d):

$$VAR = \sum_{i=1}^{n} n_i (A_i \ . \ h_i) \cdot z_d{}^{-1} A_a{}^{-1} \tag{15}$$

whereas λ_f is defined as the frontal area of the built environment over the total horizontal surface area, which is a function of the reference approaching wind direction (θ), i.e.,

$$\lambda_f(\theta) = \sum_{i=1}^{n} A_{f_i}(\theta) \cdot A_h{}^{-1} \tag{16}$$

Another important morphological parameter often used in urban energy studies is the so-called Height to Width ratio (*H/W*), which measures the aspect ratio of a characteristic street canyon. H/W in symmetrical canyons is simply calculated by dividing the uniform height of canyon walls by the width of the canyon. However, in real urban areas with complex morphologies, the majority of canyons are asymmetric. By parameterizing the streets and canyons as a function of canyon length, the *H/W* ratio is calculated for all locations of the idealized urban areas (Eq. (17)).

$$HW_{ij} = \frac{0.5\left(h_i + h_j\right) \times L_{i_1}}{W_{ij} \times L_{a_i}} \tag{17}$$

where L_i is the length of the rectangle perpendicular to the point '*ij*' on XY plane, L_{ai} is the total length of the canyon, and W is the distance between canyon buildings along the street grid. Since *H/W* ratio cannot represent the height of the all monitor points, the database of values is defined as a second-order matrix to the solver. Thus, it can only

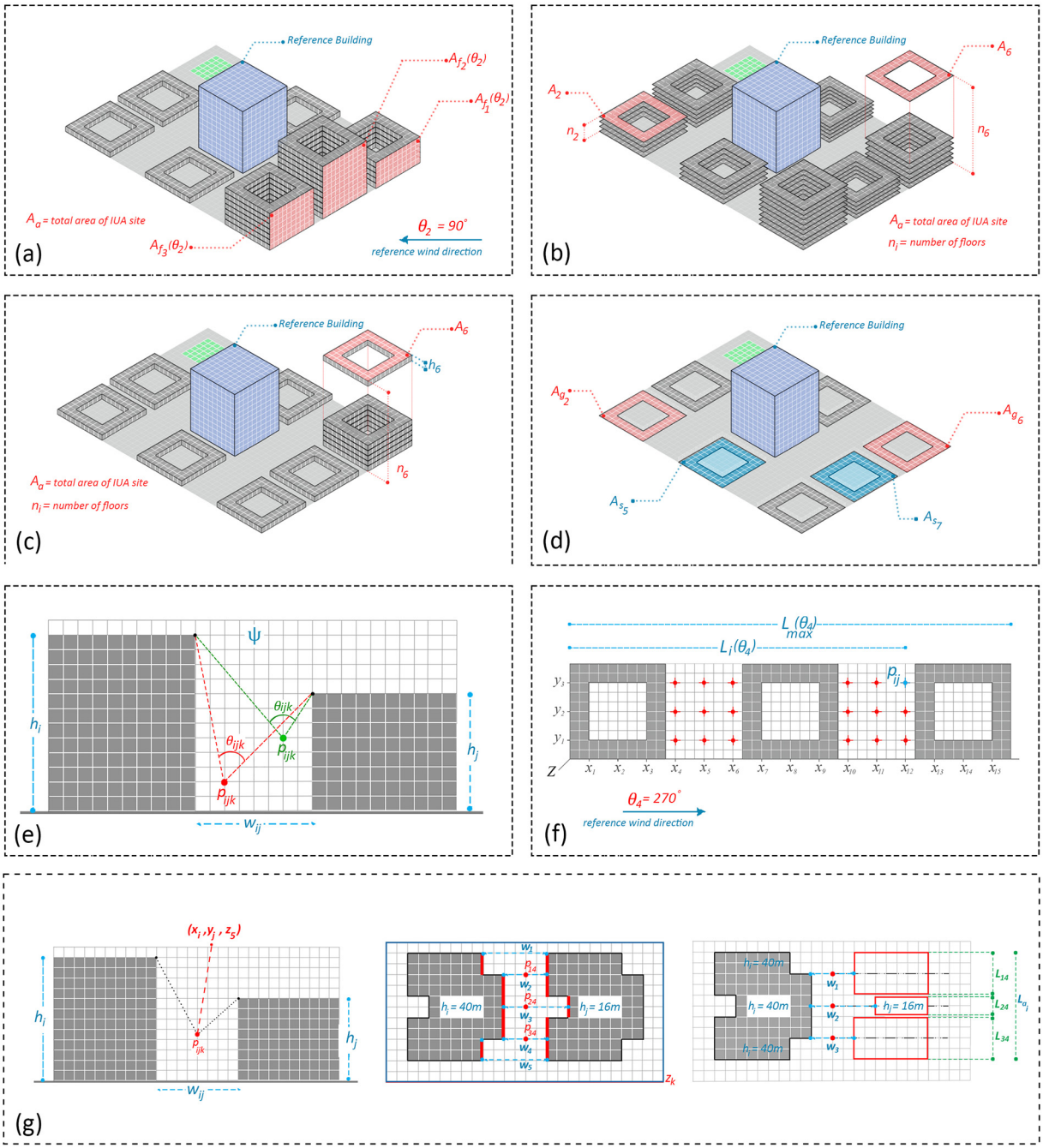

Fig. 6. Graphical representation of main morphological parameters in the developed urban morphology parameterization method: (a):λ_f (b): PAR, (c): VAR, (d): SCI, (e): SVF (Ψ), (f): Effective Length (L_e), (g): H/W ratio.

represent the urban morphology at an XY plane for monitor points located at 2 m height above the ground level. To consider the location of monitor points along the Z axis, the Sky View Factor (ψ) is also calculated for each monitor point. It defines the fraction of the overlaying hemisphere occupied by the sky at each level. Given by Eq. (18), sky view factor for a point located in a canyon is calculated as sky hemisphere visible from the point:

$$\Psi_{w_{ij}} = \left(sin^2\beta_{ij} + cos\beta_{ij} - 1 \right) \cdot \left(cos\beta_{ij} \right)^{-1} \tag{18}$$

where β is calculated using Eq. (19):

$$\beta_{ij} = tan^{-1}\left(\frac{(h_i + h_j)}{0.5W_{ij}}\right) \tag{19}$$

The Sky View Factor for this point can be calculated from Eq. (20):

$$\Psi_{p_{ij}} = 1 - 2\Psi_{w_{ij}} \tag{20}$$

Two other easy-to-calculate parameters are the coordinate of each monitor point: Normalized Height (H_n), and Effective Length (L_e). Using these two parameters, the impact of the reference wind direction can also be considered in the parameterization method. By using these two parameters, there will be no need to consider other widely-used parameters in the building energy and urban climate community such as the Roughness Length (RL) which is based on average volumetric building height, λ_f, PAR, and Surface-Averaged Drag Coefficient (C_d) of an urban site (Xu et al., 2017). RL cannot represent the specific location of monitor points and calculating C_d can be quite challenging in complex urban areas. Thus, by defining H_n

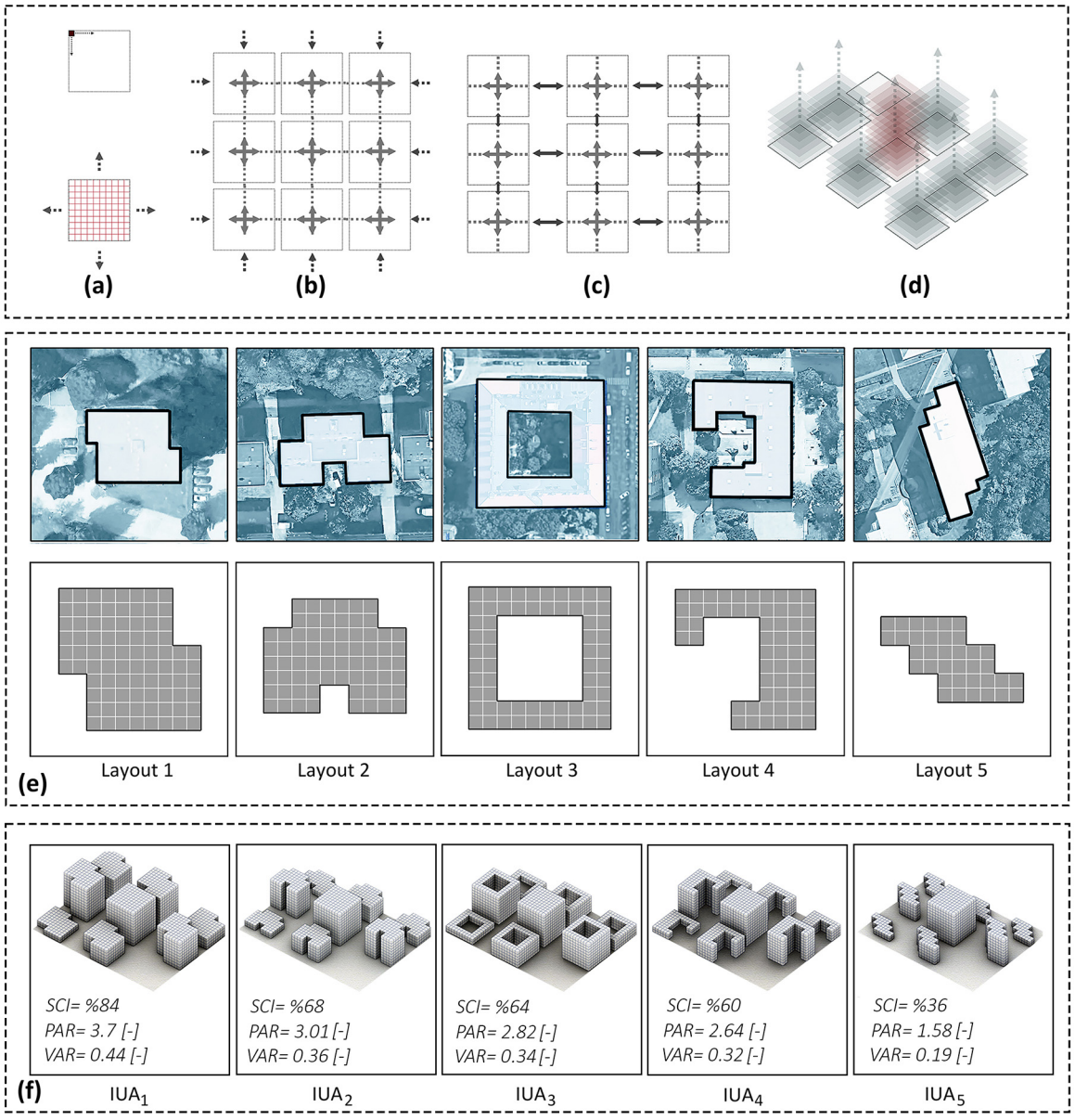

Fig. 7. Developing Idealized Urban Areas (IUAs) based on BMC technique (Javanroodi et al., 2018) (a): basic module of the 'BMC' technique, (b) modular sub-site resulting in a 9 × 9 cells, (c) horizontal expansion of sub-site for the design of urban canopies and streets, (d) vertical expansion of the developed layout for the idealized urban environments based on height distribution, (e) most frequent building layouts in the selected area, (f) resulting idealized urban areas (IUA) based on the aforementioned morphological parameters (the central building is considered as a constant form to enhance the feasibility of the comparative approach of the study).

and L_e, the morphological and aerodynamic (wind direction) characteristics of each monitor point can be represented to be used as input for NN models. H_n and L_e are calculated using Eqs. (21) and (22) respectively:

$$H_{n_i} = h_i \cdot h_{max}{}^{-1} \tag{21}$$

$$L_e(\theta_k) = L_i(\theta_k) \cdot L_{max}(\theta_k)^{-1} \tag{22}$$

here, h_{max} is the maximum height of buildings in the urban area, which is equal to 50 m in this study and θ is the reference wind direction. Moreover, L_{max} is the maximum site length, and L_i is the distance of point 'i' from the origin in respect to the corresponding wind direction.

4.2. Generating idealized urban areas

Five idealized urban areas (IUA) are generated based on the introduced morphological parameterization method adopting the "Building Modular Cell" (BMC) technique developed by Javanroodi et al. (2019). The BMC technique is based on the modular horizontal and vertical expansion of a basic 4 × 4 × 4 m^3 cube to generate building forms and complex urban morphologies based on a range of five urban densities. The application of BMC is extensively used in in urban energy (Javanroodi et al., 2018), microclimate (Javanroodi and Nik, 2020), and urban energy system (Perera et al., 2021b) studies. Here, BMC technique is further developed by selecting five most frequent architectural layouts out of 25 distinct layouts pertaining to the selected area (Fig. 7). The dimension of the selected layouts is normalized to the basic rectangular module which encompasses a 10 × 10 grid with 100 cells (each cell is a square with 4 m dimension). A regular urban area in Stockholm is an area with contiguous buildings with no more than 200 m distance between them and accommodating at least 200 residents each (Localities, 2019). The mean household size in Stockholm is 2.6 persons (2.2 persons in Sweden) and the population density is 1432 per m^2 (Localities, 2019). Thus, a 184 × 136 m^2 rectangular site is designed, covered by eight buildings, and one public open space (25,024 m^2

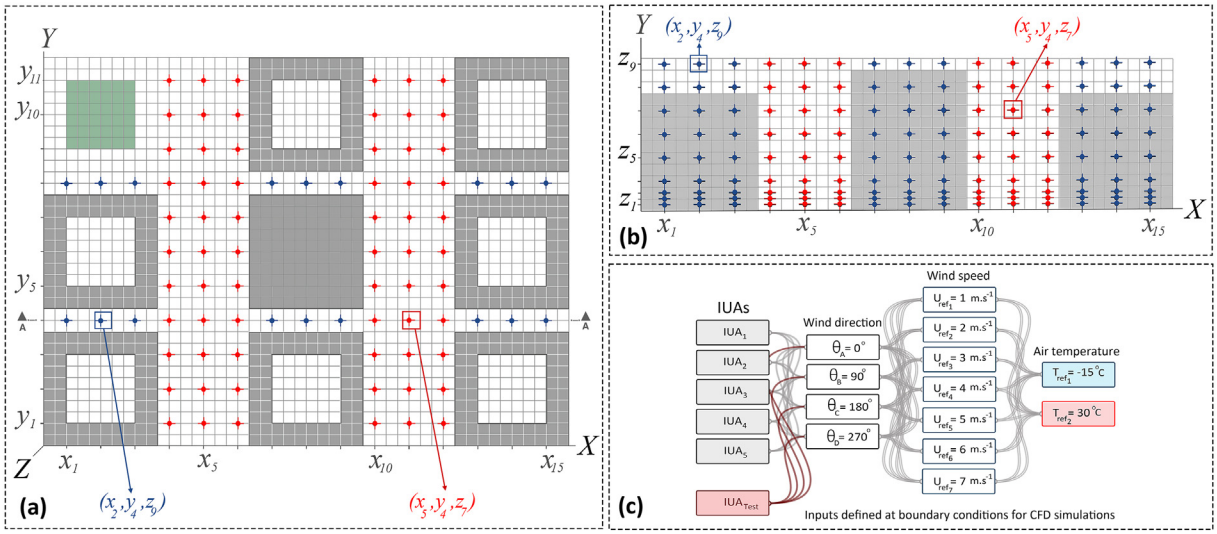

Fig. 8. (a) 84 monitor points at 2 m above ground level for Case 4, (b) a schematic section at (x_i, y_4, z_n) coordinate to show nine defined height surfaces at each location in IUA_4, (c) typical and extreme mesoscale wind speed, air temperature, and wind direction considered as reference input in CFD simulations of IUAs.

total area). A 6 × 6 m^2 green space was defined at the right corner of each site according to the average urban vegetation cover per square meter in the studied area. The total planar area fraction of buildings varies from 0.23 to 0.51. Two types of streets are considered in each urban area, including wide (32 m width) and narrow (8 m width) streets, based on the existing urban streets and canyons in the selected area. Real urban areas are typically characterized by a non-uniform building height distribution, thus the building height in the IUAs is defined based on a mixed-height distribution criterion (readers are referred to a previous paper by the authors (Javanroodi et al., 2019) for more information). The main constraint for the height distribution is the magnitudes of the *PAR* and *SCI* parameters, where IUAs with higher *PAR* and *SCI* magnitudes have a higher number of floors. Based on the average household size and population density, the minimum number of the floors in the urban areas was adjusted to a minimum of 42 (IUA with the lowest PAR and BCR) to a maximum of 66 (IUA with the highest PAR and BCR) floors. Considering at least two apartments on each floor, the minimum total number of residents in the developed urban area is not less than 218 persons with a total area of 25,000 m^2.

4.3. Adopting the verified multi-scale approach

Based on the verified convergence scenario and Standard k-ε model, for each IUA, 756 monitor points at 84 sets (each set represents a location on XY axis with 9 points at Z-axis from 2 to 55 m height above ground) in a 15 × 11 matrix are considered based on the introduced multi-scale assessment approach (Section 2.4). These monitor points are categorized based on the distance between buildings and the depth of the canyons considering both short canyons ($L/H \leq 3$) and long canyons ($L/H > 5$); where L is the length and H is the average height of canyons (Arkon and Özkol, 2014). Accordingly, in the long canyons with 32 m width 66 sets (594 points in total) and in the short canyons with 8 m width between buildings 18 sets (108 points in total) are defined. Each monitor point has a given coordinate (x_i, y_j, z_k) representing the distance of the given point from the defined origin (0,0,0). For example, the monitor point with (x_2, y_4, z_2) coordinate represents a point at the middle of the second short canyon (C_2) at 4 m height. The absolute distance between two adjacent points is 12 m, considering three sets in each short canyon and eighteen sets in each long canyons (Fig. 8-a, b). Seven reference mesoscale wind speeds (U_{ref} = 1, 2, 3, 4, 5, 6, and 7 $m{\cdot}s^{-1}$), two air temperature magnitudes (T_{ref} = −15, and 30 °C) and four major wind directions (θ = 0, 90, 180 and 270°) are considered based on climate conditions of selected area as boundary conditions in the CFD solver for IUAs (Fig. 8-c). A total number of 280 CFD simulations are conducted (56 CFD simulations per IUA) varying programmatically the input parameters (see Section 3 for input parameters). Fig. 8-c shows reference wind direction, wind speed, and air temperature values that considered in the CFD simulation of IUAs. The magnitudes of reference wind speed and air temperature represent both typical and extreme mesoscale weather conditions. Fig. A.1-b in Appendix A shows the defined computational domain and boundary conditions for the considered IUAs.

The evaluation of microclimate in the IUAs is done through mean profiles of wind speed and air temperature against z/h (height of monitor point divided by average height of buildings at each IUA). Moreover, Richardson number profiles are also used to assess the discern simulations based on their degree of convectiveness. The calculation of Richardson number is a dimensionless quantity that determines the ratio of buoyancy to shear production of turbulence, and is defined via Eq. (23):

$$Ri_{grad} = \frac{(g/T_v)(\partial\theta_v/\partial z)}{(\partial u/\partial z)^2 + (\partial v/\partial z)^2} \tag{23}$$

where g is the gravitational acceleration (set as 9.8 $m{\cdot}s^{-2}$), T_v is the absolute temperature, z is the height above ground level, and u and v are the horizontal wind components.

5. Developing CFD-NN prediction models

To capture the non-linear relationship between the considered urban canopy geometries and climate variables, two NN models, namely MLP ? thyc = 5? > and DNN models, are considered with different architectures (e.g., number of hidden layers, neurons, and features). The MLP model is developed via the Scikit-learn Python library (Varoquaux et al., 2015), whereas the Deep Neural Network (DNN) model is based on TensorFlow (TensorFlow White Papers, n.d.). The structure of the developed feed-forward model is based on using an MLP network with one hidden layer (Fig. 9-left), which is a supervised learning algorithm based on Error Backpropagation to train on a dataset and a set of features as $X = x_1, x_2, \ldots, x_m$. MLP learns the function $f(x)$ given by Eq. (24):

$$f(x) = w_{i+1}\, g\left(w_i^T x_m + b_i\right) + b_j \tag{24}$$

here w_i is the ith weight of input and hidden layers, and b_i is bias added to the ith hidden layer and b_j is bias added to the output layer. The weights

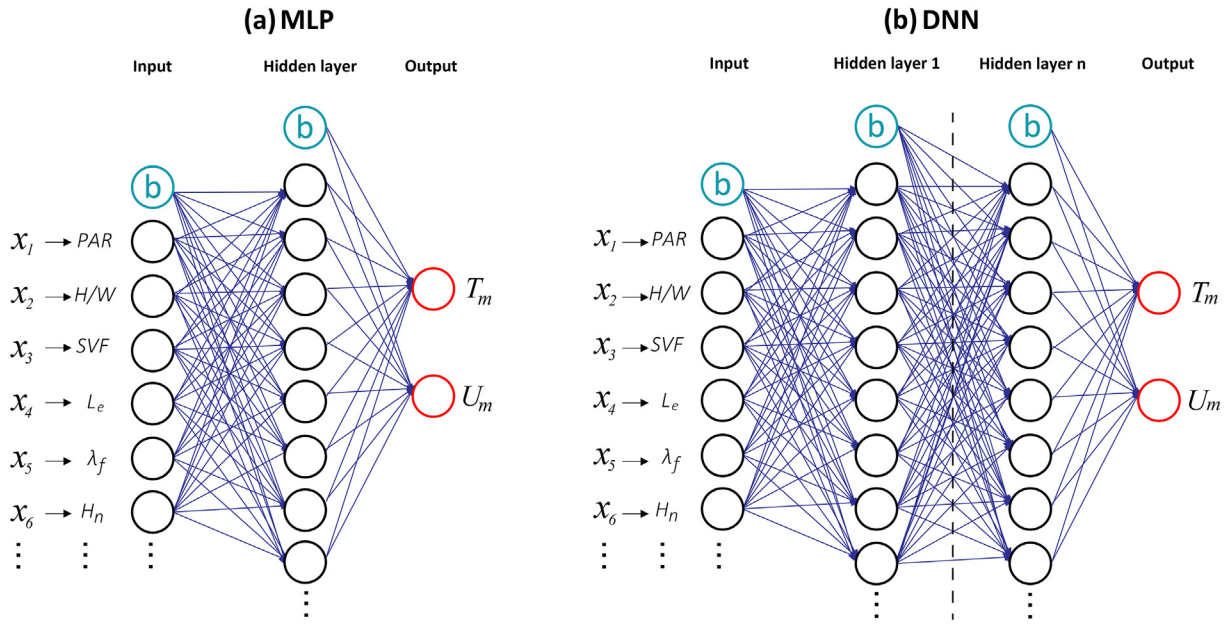

Fig. 9. Architecture of the developed MLP (left) and DNN (right) models.

and biases are applied to the inputs and pass an activation function $g(\cdot): R^m \rightarrow R^o$, where m and o are the number of dimensions of inputs and output. Two activation functions including a sigmoid with a range from 0 to 1 (Eq. (25)) and hyperbolic tangent (tanH) with a range from -1 to 1 (Eq. (26)) are deployed in the MLP model as:

$$g(z) = \frac{1}{1+e^z} \tag{25}$$

$$tanh\,(z) = \frac{e^z - e^{-z}}{e^z + e^{-z}} \tag{26}$$

Adopting random initial weights, MLP minimizes the Square Error Loss Function (Eq. (27)) via iterative update of the weights (w_i), i.e.,

$$Loss(\hat{y}, y, w) = \frac{1}{2}||\hat{y} - y||_2^2 + \frac{\alpha}{2}||w||_2^2 \tag{27}$$

Using Gradient Descent with Momentum (GDM) optimization algorithm the estimated weights are updated using Eq. (28):

$$w_{i+1} = w_i - \eta_k \nabla Loss_i^w + \alpha \Delta w_i \tag{28}$$

here, η_0 is the learning rate parameter (initial learning rate set as 0.4), and α is the momentum rate (set as 0.9). Additionally, adopting the Permutation Feature Importance function, the model dependency to the selected features is indicated.

Due to complex interactions between morphological parameters and microclimate variables, a single layer might not be able to capture all non-linearities, and two or more hidden layers are often used to better capture complex non-linear interactions (Basheer and Hajmeer, 2000). The error terms of back propagation in MLP networks might decrease by adding more hidden layers (Panchal et al., 2011). However, complex multilayer MLP models with redundant hidden layers can lead to overfitting (Rynkiewicz, 2012). Thus, two standard deep neural networks are also developed with two and three hidden layers (Fig. 9-right). In the developed DNN models based on (Sweden's National Report for the third United Nations Conference on Housing and Sustainable Urban Development (Habitat III). Swedish National Report, n.d.), the non-linear and linear transformations are composed at each level, followed by the connected neuron of the output layer via Eq. (29):

$$\alpha = \sum_{i=1}^{n} \omega_i x_i + b_i \tag{29}$$

where x_i is the input, ω_i is the weight, b is the bias and α is the output variable. The DNN model minimizes the error between predictions and the target outputs by updating the weights and biases (w and b) via an optimization algorithm based on back propagation. The activation function for the hidden layers is the Rectified Linear Unit (ReLU) and for the output layer is set to softmax as recommended by several research works with similar structure due to better performance and efficiency (Su et al., 2017; Achieng, 2019). ReLU and softmax activation functions are expressed using Eqs. (30) and (31) as following:

$$relu(\alpha) = max\,(0, \alpha) \tag{30}$$

$$softmax(\alpha) = \frac{e^{\alpha_i}}{\sum_j e^{\alpha_j}} \tag{31}$$

For each iteration, the loss function partial derivative values are calculated for each input parameter. The Adaptive Moment Estimation (ADAM) algorithm is used as optimizer.

Table 1
Configuration used for MLP and DNN prediction models.

Models	No. of hidden layer	No. of neurons	No. of features	Activation functions	Optimizer
MLP	1	[10, 15, 20, 25, 30]	[9, 8, 7, 6]	[Sigmoid, tanH]	[SGD]
DNN	2	[10, 15, 20, 25, 30]	[9, 8, 7, 6]	(ReLu, softmax)	[Adam]
	3	[10, 15, 20, 25, 30]	[9, 8, 7, 6]	(ReLu, softmax)	[Adam]

For both models, different data segment partitions are examined for the training sets. To achieve optimal performance, a different number of neurons, hidden layers, and features are also examined (Table 1). The models are trained on the database of CFD simulation (wind speed and air temperature), and nine morphological parameters as features (*PAR*, *VAR*, *H/W*, λ_f, L_e, H_n, *SVF*, X, and Y coordinates).

The performance of each model with corresponding configurations is assessed in Section 6.2. To assess the performance of the prediction models, the Root Mean Square Error (RMSE), and R-squared (R^2) are calculated using Eqs. (32) and (33) respectively via the Scikit-learn library.

$$RMSE = \sqrt{\frac{1}{N}\sum_{i=1}^{N}(\hat{y}_i - y_i)} \tag{32}$$

$$R^2 = 1 - \frac{\sum_{i=1}^{N}(y_i - \hat{y}_i)^2}{\sum_{i=1}^{N}(y_i - \bar{y})^2}, \bar{y} = \sum_{i=1}^{N} y_i \tag{33}$$

6. Results and discussion

The impact of urban morphology on the fluctuations of climate variables are investigated for typical and extreme weather conditions in Section 6.1. The interactions between climate variables in all IUAs are assessed using a conventional multi-linear regression model. The performance of the developed CFD-NN models in predicting climate variables is assessed in Section 6.2. Section 6.3 examines the accuracy of the developed model in predicting urban microclimates of an unseen urban morphology across a range of forcing conditions. Limitations of the proposed study follow in Section 6.4.

6.1. Interactions between climate variables and urban morphology

This section aims to characterize the relation between climate variables (wind speed, turbulence components, and air temperature) and urban morphology. Wind speed variations and air temperature across the considered urban areas are assessed using mean profiles for short and long canyons over UCL (average of all monitor points considering mean wind velocity in all directions) for all IUAs (Fig. 10). Figs. A.3 and A.4 in Appendix A show wind velocity and air temperature plan-view CFD at 2 m with $U_{ref} = 1\ m{\cdot}s^{-1}$ and $T_{ref} = 30\ °C$. Assessing mean profiles and CFD contours show that the inflection point in each IUA is a function of urban morphology, which varies with the value of reference wind direction and complexity of the building forms. For example, for reference wind directions $\theta = 0°$ and 180°, the flow is channeled along long canyons which amplifies the wind speed at the near ground surfaces. On the contrary, when the approaching flow is perpendicular to the long canyon's axis (θ = 90 and 270), the airflow is blocked by the windward buildings and a cavity-like regime characterizes the street canyon. While the majority of studies with uniform building height reported a direct relation between density-based parameters and velocity gradient (Abd Razak et al., 2013; Kono et al., 2010), no apparent trend is found in our cases, which feature buildings of variable height and a relatively rich morphology.

With $\theta = 0°$ and $U_{ref} = 1\ m{\cdot}s^{-1}$, in the case of $IUA_{3,4,5}$, the wind speed is constant from 0.03 to 0.14 z/h in short canyons, while in $IUA_{1,2}$ due to higher shear stress, the slope of vertical shear rate is notably higher. In the case of long canyons, this condition can be only seen in IUA_1, whereas the slope of wind gradient is notably larger in θ = 0, and 180° due to the channeling flow effect. The shear stress in urban areas such as IUA_2 and IUA_3 with more complex building forms is not sensitive to variations in the approaching wind direction. Nevertheless, compared to the short canyons, the local vertical average shear rate due to the dominant shear stress at the bottom of long canyons. In all IUAs, the inflection point can be seen from z/h of 0.25 to 0.35 (where h is the average height of IUA). The highest deviation difference between normalized wind speed magnitudes in long canyons is less than 3% for all four corresponding wind directions with few exceptions such as IUA_2 in θ = 90° (5%), and IUA_5 in θ = 0 and 180° (8% and 11%).

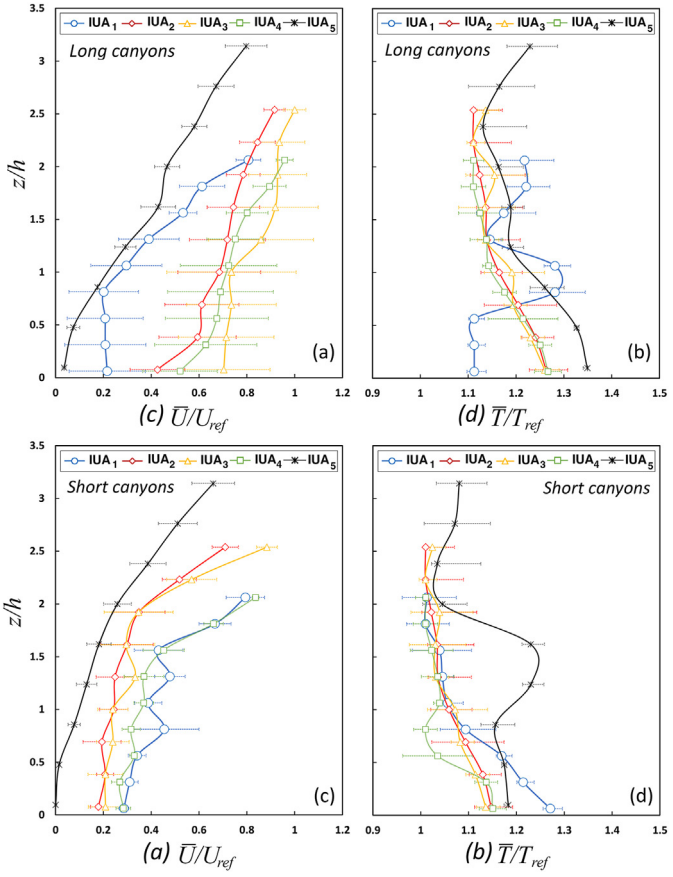

Fig. 10. Mean wind speed and air temperature profiles for long (a, b), and short canyons (c, d) based on normalized magnitudes (U_{ref} = 2 m·s^{-1}, T_{ref} = 30 °C). Error bars showing the variation of climate variables based on four wind directions (θ = 0, 90, 180, 270°).

For short canyons, the flow pattern of the wind speed is affected by the variations of the surface roughness that amplify the upstream flows. For example, with $\theta = 0°$ (where only C_1 can be considered as windward); the highest wind speed magnitude near ground surface (z/h less than 0.15) is observed in $IUA_1$and IUA_4 with the highest roughness and semi-cuboid forms. This is due to the lower distance between B1 and B2 buildings (8 m) compared to the other three IUAs; which results in lower wind speed amplification. To better understand the impacts of short/long canyons on the vertical gradient of wind speed at each IUA, Fig. A.3 in Appendix A shows mean wind speed profiles at five different sets of monitor points based on normalized values (U_{ref} = 5 m·s^{-1}, and $T_{ref} = -15\ °C$).

A closer look into the air temperature contours in the short canyons shows considerably lower temperatures compared to long canyons (see Fig. A.5 in Appendix A comparing normalized mean wind profiles in three calculation sets located in the wider streets). For example, with θ = 180° approaching wind in IUA_4 (with 64% site coverage and courtyard forms) the air temperature below z/h = 0.69 is notably higher in C_5 compared to C_6 (which is closer to the approaching wind speed). The same phenomenon can be seen in $\theta = 0°$ between these two canyons as well as θ = 90 and 270°; where in θ = 90°, the air temperature at the selected canyons is lower due to higher wind speeds compared to θ = 270°. The highest air temperature over UCL is observed in IUA_5 with the lowest built density. This is due to the low amount of shading and low average wind speed over UCL in IUA_5. However, higher microscale wind speed can result in lower temperature by improving thermal circulation; particularly in short canyons.

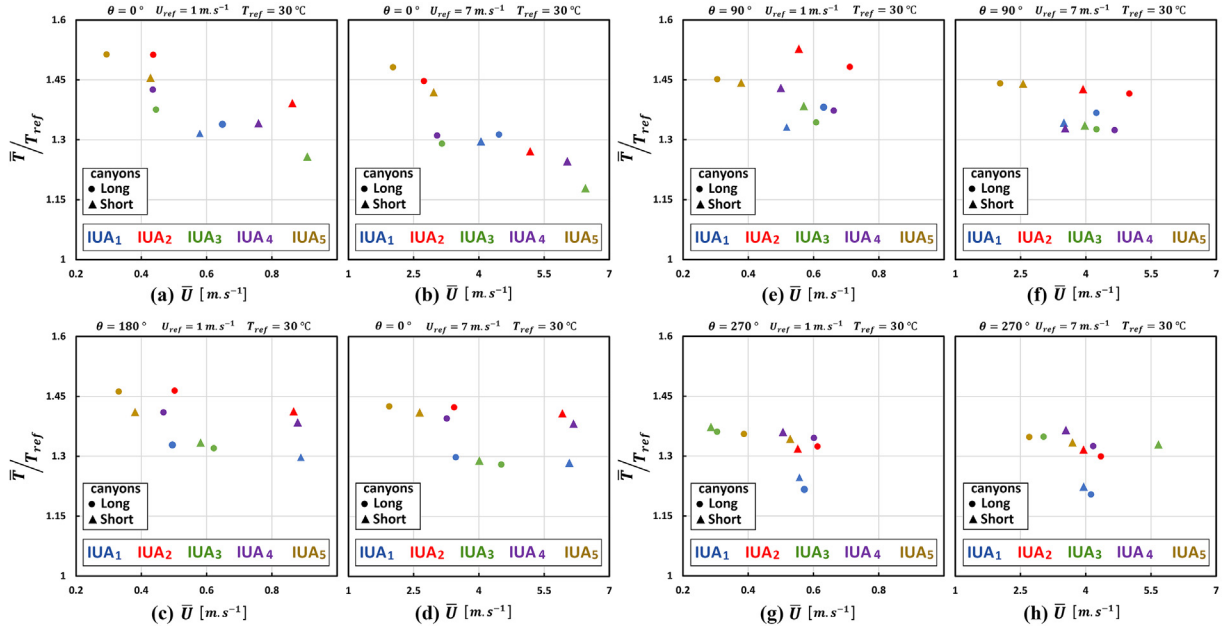

Fig. 11. Average wind speed (U_{ref} = 1 and 7 m·s^{-1}) as a function of average normalized air temperature (T_{ref} = 30 °C) at microscale.

The mean wind speed and air temperature profiles imply lower wind speed variations as a function of height with higher reference wind speeds (e.g. U_{ref} = 3–7 m·s^{-1}) due to larger flow gradients near the ground surface as a result of reverse vortices. However, it is important to assess how thermal stratification affects turbulence production and flow regime at each IUA. Thus Fig. A.6 shows a plot of Gradient Richardson number as a function of height (z/h) for U_{ref} = 1 m·s^{-1} (left panel) and 7 m·s^{-1} (right panel) using average wind velocity components (u, v) and potential temperature (θ_v) over UCL, which is used in meteorology to characterize the dynamic stability of a stratified flow. The vertical line on the graphs shows the magnitude of the Critical Richardson number (Ri_c = 0.25), that denotes the value below which a statistically uni-dimensional stratified shear flow will be unstable to small perturbation. According to the results, with U_{ref} = 1 m·s^{-1}, the flow regime is mostly stable under z/h = 1, except for IUA_1 and IUA_4 with Ri less than 0.25 at z/h = 0.3 to 0.6. However, with U_{ref} = 7 m·s^{-1} the Ri_{grad} remains under the Ri_c throughout the UCL, except for IUA_5. A similar condition can be seen in IUA_2 under z/h = 1 with both low and high reference wind speeds. The value of Ri_{grad} decreases by height in IUA_5, whereas at the top of the canopy (z/h = 2.5) the Ri_{grad} is always less than 0.1.

Another important aspect of microclimate assessment is quantifying the interactions between wind speed and air temperature. Linear regressions are evaluated between average wind speed and average air temperature (out of all monitor points) over UCL in all IUAs. Generally, a weak linear correlation is observed between average wind speed and air temperature in the short and long canyons. Except for IUA_5 in θ = 0, 90, and 270° (with R^2 of 0.71, 0.87, and 0.91 respectively), no significant correlations are observed in other IUAs ($R^2 < 0.74$). We also present a linear regression analysis to highlight relations between the averaged (all monitor points) U_m, and T_m and the morphological parameters (*PAR*, *VAR*, λ_f, *H/W*, *SVF*, L_e, H_n, X, Y). The value of R^2 for wind speed and air temperature using MLR models are 0.21 and 0.35 respectively. Thus, no general rule can be derived out of the results based on the variation of IUAs or reference wind direction using linear regression models. In terms of average values (out of all monitor points), the highest average air temperature in both long and short canyons can be seen in IUA_5 with the lowest average wind speed magnitude located in the near the ground surface, and probably the result of low shading (Fig. 11). In this IUA, mean wind speed tends to converge to the reference wind speed from 26 m height to higher elevations; however, due to lower shear stress near the ground surface, a higher average wind speed is observed in the short canyons. Although linear regression analysis based on average values can present an overview of microclimate conditions in each IUA, no generalized linear relation can be derived out of the results, even for IUA_5.

Table 2
Performance indicators for different number of neurons in the two considered CFD-NN prediction models: MLP with one hidden layer and DNN with two hidden layers.

Units	Target	MLP				DNN			
		R^2		RMSE		R^2		RMSE	
		Train	Test	Train	Test	Train	Test	Train	Test
10	U_m	0.66	0.59	0.128	0.146	0.81	0.78	0.087	0.087
	T_m	0.81	0.76	0.094	0.109	0.91	0.84	0.068	0.081
15	U_m	0.82	0.73	0.076	0.112	0.85	0.81	0.082	0.08
	T_m	0.88	0.85	0.072	0.081	0.92	0.89	0.061	0.068
20	U_m	0.88	0.78	0.087	0.091	0.89	0.83	0.071	0.086
	T_m	0.90	0.87	0.068	0.074	0.92	0.89	0.059	0.073
25	U_m	0.88	0.81	0.076	0.0	0.91	0.86	0.067	0.078
	T_m	0.90	0.87	0.076	0.073	0.93	0.92	0.057	0.062
30	U_m	0.88	0.81	0.074	0.079	0.91	0.87	0.065	0.076
	T_m	0.91	0.86	0.069	0.079	0.93	0.92	0.057	0.062

Table 3
Impacts of different number of hidden layers on the performance of two CFD-NN prediction models.

NN models	No. of hidden layer	U_m				T_m			
		R^2		RMSE		R^2		RMSE	
		Train	Test	Train	Test	Train	Test	Train	Test
MLP	1	0.88	0.84	0.076	0.081	0.91	0.88	0.071	0.077
	2	0.87	0.84	0.075	0.080	0.91	0.88	0.071	0.077
DNN	2	0.89	0.87	0.071	0.074	0.93	0.92	0.057	0.061
	3	0.91	0.89	0.067	0.071	0.94	0.92	0.049	0.061

Table 4
Impacts of different training-test ratios on the performance of prediction models.

Training set ratio [%]	Model	U_m		T_m	
		R^2	RMSE	R^2	RMSE
70	MLP	0.88	0.076	0.91	0.065
	DNN	0.91	0.065	0.94	0.051
60	MLP	0.84	0.081	0.89	0.071
	DNN	0.91	0.067	0.94	0.052
50	MLP	0.79	0.090	0.81	0.087
	DNN	0.87	0.074	0.92	0.061

6.2. Developing a hybrid CFD-NN prediction model

As discussed in Section 5, two NN microclimate prediction models (with MLP and DNN architectures), are developed to capture the non-linear relationships between climate variables and urban form, based on the previously defined morphological parameters. In this section, we first carry out a sensitivity analysis to identify the optimal network architecture (number of hidden layers, neurons, data segmentation ratio, activation, and optimization functions). Architectures comprising 5 to 30 neurons are assessed here in terms of RMSE and R^2 considering three different train-test split ratios (Table 2). According to the results, no sensible variations in the predictive capacity of the MLP network occur beyond 20 neurons and one hidden layer (R^2 = 0.88 and 0.90 for wind speed and air temperature, respectively). It is important to note that a higher number of neurons can negatively affect the out-of-sample predictive capabilities of the model (overfitting). A similar analysis was carried out for the DNN model, and the final architecture consisted of 25 neurons distributed between two hidden layers (R^2 = 0.91 and 0.93 for wind speed and air temperature, respectively).

In an attempt to improve the accuracy of the NN models, a hidden layer with the same number of optimal neurons is added to both models. Although no significant improvement was observed for the MLP model,

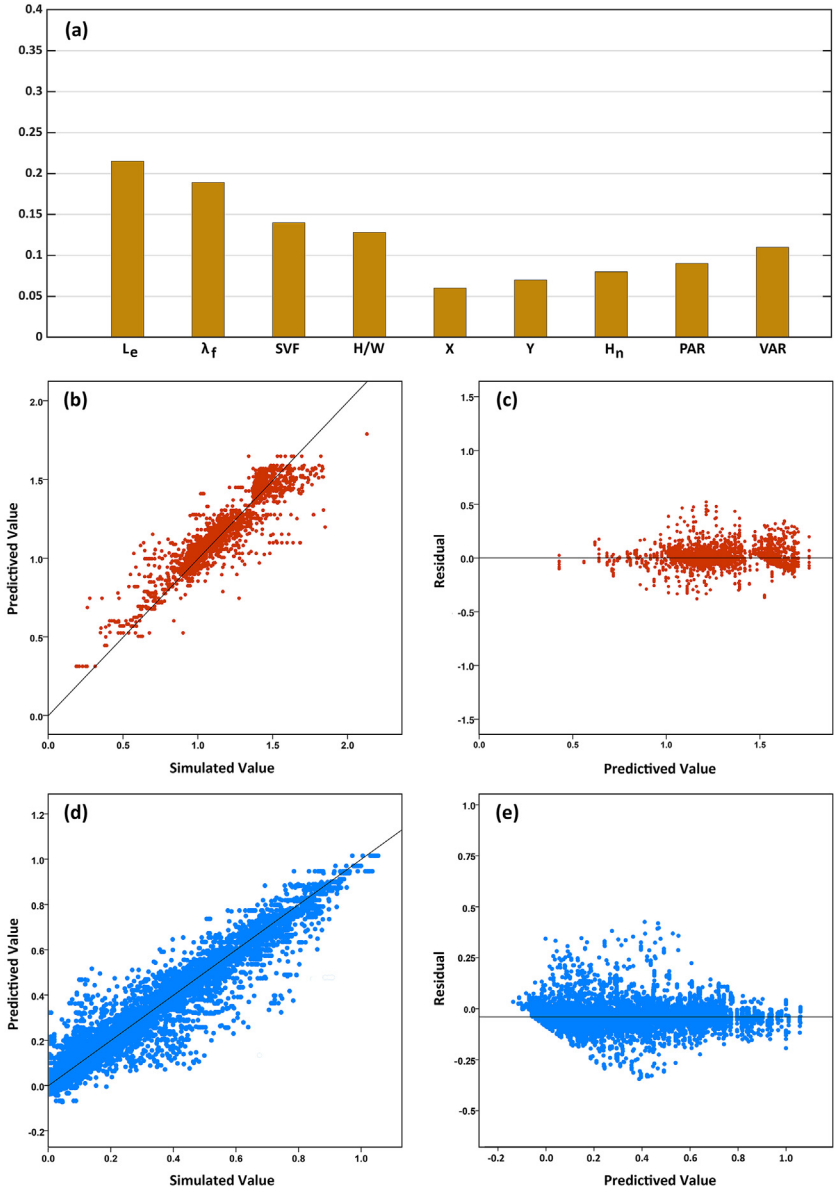

Fig. 12. Permutation feature importance analysis considering nine morphological parameters (a), the result of CFD-NN prediction model adopting DNN for temperature (b) and wind speed (c) at microscale considering all monitor points.

Table 5
The performance of developed CFD-NN models in predicting wind speed and temperature.

Best models	U_m		T_m	
	R^2	RMSE	R^2	RMSE
MLP	0.88	0.076	0.91	0.065
DNN	0.91	0.065	0.94	0.053

modest variations (less than 0.02 improvement of R^2) were observed for the DNN model with three hidden layers (Table 3).

An important consideration for a NN model is its capability to generate good predictions when trained with scarce datasets. This could be even more important for microclimate studies, which suffer from the lack of long-term and spatially distributed measurements. Here, the optimal models were trained based on three different train-test split ratios. The dataset is randomly divided into training and test subsets by 70/30, 60/40, and 50/50 split (Table 4). Results show that both MLP and DNN models are capable of learning and predicting wind speed and temperature to an acceptable degree of accuracy. The value of R^2 in the MLP model with a 60% training ratio is only decreased by a few percentage points when compared to the 70% training subset for wind speed and air temperature respectively. The value of R^2 for MLP model with train/test split ratio of 50%–50% decreases by 0.09 and 0.10 for wind speed and air temperature respectively compared to optimal model (with train/test split ratio of 70%–30%). This is while the DNN model showed a satisfactory performance with a train/test split ratio of 50%–50% split ratio; showing reliable predictions for both wind speed and air temperature.

The importance of each feature (morphological parameters) is also assessed for both prediction models by conducting a sensitivity analysis using the Permutation Importance function in the Scikit-learn Python library. Here, the importance of features is computed considering both training and testing datasets. Specifically, the values of each feature are shuffled, and its impact on the loss function variations and performance deterioration of the NN model is assessed. This procedure is repeated for all nine features. According to the results, six predictors including L_e (0.21), λ_f (0.18), SVF (0.14), H/W (0.12), VAR (0.11), X (0.06), and Y (0.07) showed the highest importance in determining NN models (Fig. 12-a). These predictors are selected as features for the best performance prediction models. Predictions from the CFD simulations of the cases are inter compared against corresponding results from the best performance DNN model in Fig. 12-b, c. The DNN model features an $R^2 = 0.91$, (RMSE = 0.065) for wind speed, and $R^2 = 0.94$ (RMSE = 0.053) for air temperature, which can be considered as satisfactory for most urban microclimate applications. The MLP model also showed a comparable accuracy without taking elapsed training time into consideration, with a R^2 of 0.88 (RMSE = 0.076) for wind speed and R^2 of 0.91 (RMSE = 0.065) for air temperature. The training time for the DNN model showed two times speedup compared to the MLP model. Although the training time for IUAs in this study is not significant (<1 h for the MLP model), a faster training time can be immensely helpful for real

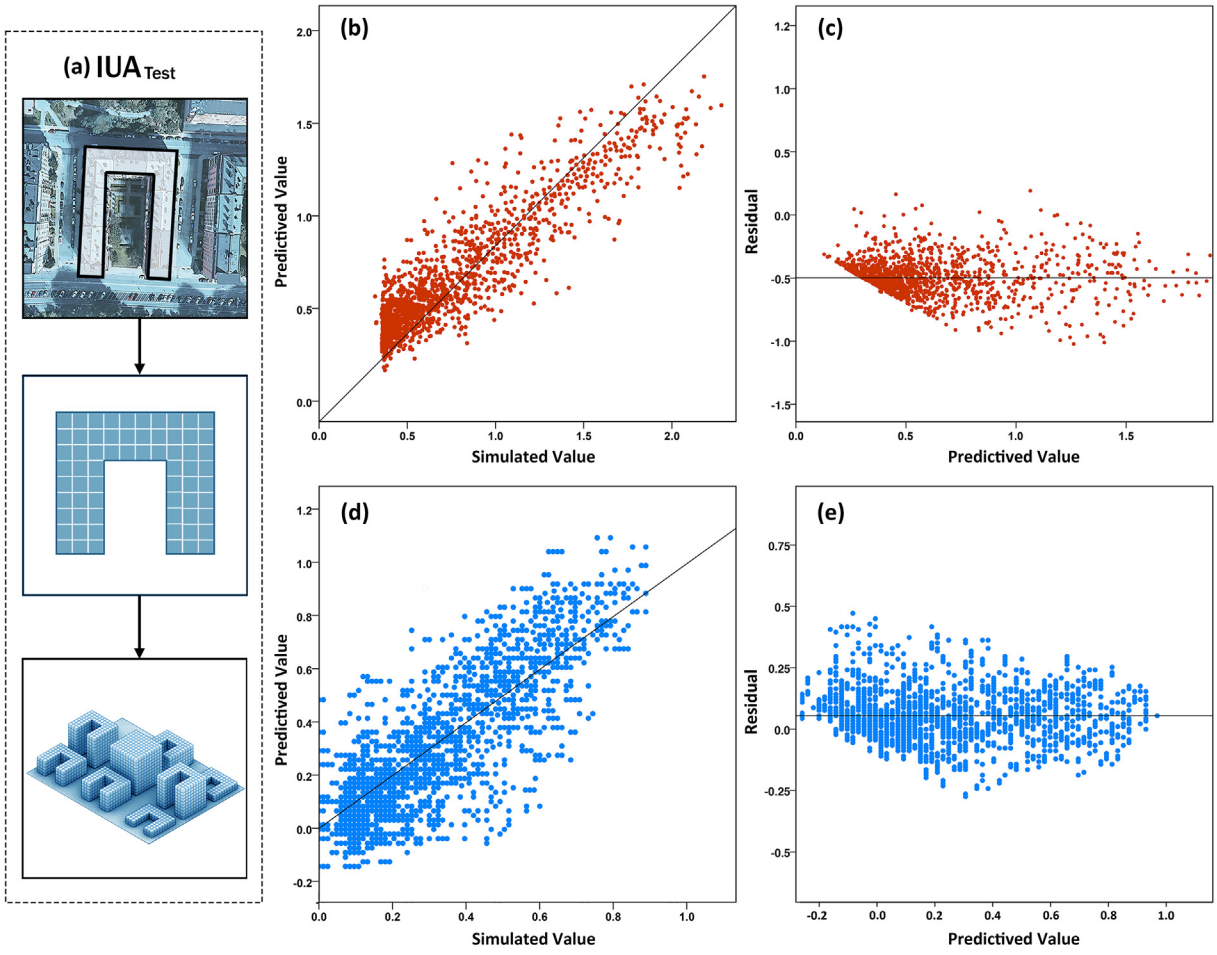

Fig. 13. Left: a new IUA to test the performance of developed CFD-NN prediction model for a new set of data, Right: results of CFD-NN prediction model adopting DNN for temperature and wind speed in IUA_{Test}.

Table 6
The performance of developed CFD-NN models in predicting wind speed and temperature in IUA_{test}.

CFD-NN models	IUA_{test}			
	U_m		T_m	
	R^2	RMSE	R^2	RMSE
MLP	0.67	0.129	0.74	0.116
DNN	0.74	0.115	0.81	0.094

complex urban morphologies with larger areas and larger degrees of scale separation. Results showed that both of the developed NN models are reliable and capable of capturing non-linear interactions between urban form, wind speed, and air temperature profiles (see Table 5).

6.3. Deploying CFD-NN model for a new case

An important aspect of NN-based prediction models is their capability to yield good predictions beyond the training data. In this section, the MLP and DNN models are deployed to predict wind speed and air temperature over and within a new urban morphology. A new IUA is generated (Fig. 13-a) based on the parameterization method described in Section 4 (referred to as IUA_{Test}). The verified multi-scale assessment approach (Section 4.3) is defined for the IUA_{test} with 759 monitor points. A total number of 56 new CFD simulations are conducted using the verified CFD model (Section 2.4) for seven reference wind speeds (U_{ref} = 1 to 7 $m{\cdot}s^{-1}$) in two extreme air temperatures (T_{ref} = −15, 30), and four approaching wind directions (θ = 0, 90, 180, 270). The normalized database of CFD simulations is considered as the ground truth for the NN validation effort. The developed prediction models are used to predict mean wind speed and air temperature where averaging is performed over the previously introduced monitor points.

Both models showed an acceptable performance in predicting air temperature compared to CFD simulation results (see Table 6). The value of R^2 and corresponding RMSE for the MLP network in predicting air temperature is 0.74 and 0.116 respectively, whereas the DNN model showed a slightly better performance in predicting air temperature with R^2 of 0.81, and RMSE of 0.094. In terms of wind speed, both prediction models showed a slightly lower accuracy, with an R^2 value of 0.74 (RMSE = 0.115) for the DNN model, and R^2 = 0.67 (RMSE = 0.129) for the MLP one, respectively. Fig. 13-b–e contrasts CFD with NN values for the DNN model in terms of both air temperature and wind speed for this test case. Discrepancies

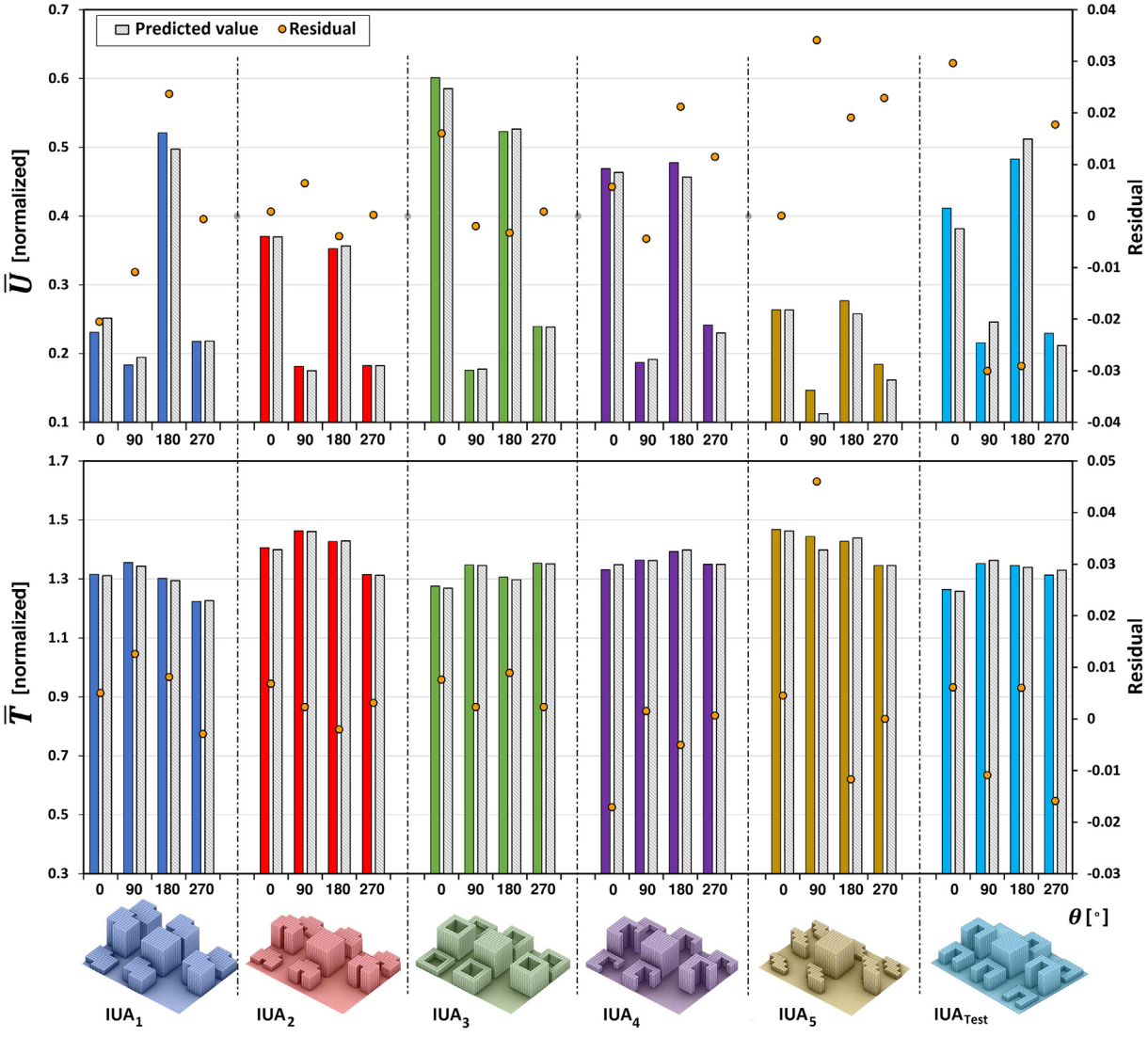

Fig. 14. The performance of CFD-NN prediction model adopting DNN in predicting average (all monitor points) wind speed (top), and temperature (bottom) in all six IUAs.

between the NN and CFD results are particularly apparent for low wind velocity, which might pertain to convective flow regimes, thus highlighting that these regimes could be a potential challenge for NN models, at least for the considered geometries. Overall, based on our study, the explanatory capabilities of the NN models can be considered as satisfactory for typical microclimate studies with respect to building energy performance analysis. It should be noted that the predictions are solely based on morphological parameters that are pertinent to building energy studies.

Fig. 14 compares the values of average site temperature and wind speed averaged over the monitor points for the DNN model and across the considered IUAs. The developed model shows an good performance in predicting the average wind speed and air temperature magnitudes. In IUA_{1-5}, the model predicts average wind speed and air temperature respectively with less than 8% and 3% relative error. It should be noted that no specific trend can be observed based on wind direction magnitude. For example, in IUA_2, the most accurate air temperature predictions are seen at $\theta = 180^{\circ}$ with less than 1% relative error. For IUA_{Test} the predictions show a lower accuracy with up to 11% and 5% relative error for wind speed and air temperature. Here, the relative error in predicting average wind speed magnitudes are 7%, 11%, 6% and 3% at $\theta = 0, 90, 180, 270^{\circ}$ respectively. These values for average air temperature magnitudes are 1%, 2%, 2% and 5%. All in all, considering spatial prediction based on 759 monitor points individually and average magnitudes of wind speed and air temperature out of all monitor point, the developed CFD-NN model in this study is proven to show an accurate and reliable performance over the considered urban parameter space.

6.4. Limitations of the study

This study had several limitations in terms of the adopted methods. The idealized urban areas developed in this study (with about 24,000 m^2 total area) are not necessarily encompassing all possible urban geometries. This most likely limits the validity of model predictions to the considered parameter space and possibly to geometrically-similar urban morphologies. Further investigation is required to account for more complex urban forms (e.g., non-rectangular layouts, roof forms, etc.) in the parameterization methods. The first step of the study evaluated a real site in Stockholm for three days and at an hourly resolution to represent typical and extreme weather conditions. However, a higher number of numerical simulations are required to account for the possible range of urban climates variabilities at the microscale.

Considering a higher number of wind directions would also result in more accurate prediction models. Finally, due to the complex nature of the problem, this study only focused on predicting wind speed and air temperature. Relative humidity, mean radiant temperature, and surface temperature also play a major role in controlling urban climate and the performance of building energy models and their impact has not been considered in this work.

7. Conclusions

This research proposed a hybrid model to predict the interactions between climate variables and urban morphology by coupling Computational Fluid Dynamics with Artificial Neural Networks. A two-equation turbulence model (Standard k-ε) and a zero-equation turbulence model (algebraic eddy-viscosity) were compared against in-situ measurements. An urban parameterization method was developed based on morphological parameters that are relevant for building energy studies, and five idealized urban areas were generated accordingly. Adopting the verified CFD model and the urban canopy parameterization, the vertical structure of the mean wind speed and air temperature from mesoscale to microscale was quantified over and within idealized urban areas. The microclimate and morphological databases were fed into two artificial neural network models, including a Multilayer Perceptron (MLP) and a Deep Neural Networks (DNN) to predict wind speed and air temperature magnitudes. The DNN model with three hidden layers outperformed the MLP model in both training and testing datasets with a Root Mean Square Error (RMSE) of 0.065 and 0.053 for normalized wind speed ($R^2 = 0.91$) and air temperature ($R^2 = 0.94$). The best performance prediction models were deployed to test their reliability and accuracy in assessing a new set of morphological data. Results showed an acceptable accuracy with RMSE of 0.115 and 0.094 for normalized wind speed ($R^2 = 0.74$) and air temperature ($R^2 = 0.81$). The model also showed a satisfactory performance in predicting average site wind speed and air temperature (out of all monitor points) with low relative errors (-11% and $+5\%$, respectively).

The proposed model is relatively efficient compared to its CFD counterpart and shows promising potential for predicting microclimate conditions in urban environments. This highlights the great this approach for urban energy studies, especially when considering that the present state of the art in linking microclimate and urban energy performance (through an integrated workflow) is focused solely on air temperature (e.g., urban energy balance equations). Additional variables such as relative humidity, surface temperature can be also readily incorporated in to the introduced model to enhance the reliability of building energy performance simulations and urban comfort studies. The model can also be used for making more informed design decisions at early stages to improve the climate-resilience of urban energy solutions. This can be critical when considering the impacts of climate change, that will introduce more frequent and larger extreme weather events, with consequences on the energy performance of buildings as well as on urban comfort. The proposed prediction model shows good promise in terms of accuracy and generalizability, and be readily deployed to estimate microclimate-related variables across urban areas within the range of the considered parameter space. This study also provided an insight into the vertical structure of mean wind speed and air temperature when downscaling from the mesoscale to the microscale across a range of urban morphologies, which can be used to study urban comfort at the pedestrian level and building energy performance at the urban scale. As a future outlook, the application of the developed urban morphology parameterization method and prediction model can be further extended to more complex urban areas. More than that, the developed method has the potential to be integrated into existing visual programming language platforms (i.e., Grasshopper, Dynamo, etc.) to be coupled with widely-used energy simulation engines (i.e., EnergyPlus, CitySim Pro, etc.)

CRediT authorship contribution statement

Kavan Javanroodi: Conceptualization, Methodology, Software, Validation, Investigation, Writing – original draft, Visualization. **Vahid M. Nik:** Methodology, Writing – review & editing, Funding acquisition. **Marco Giometto:** Methodology, Writing – review & editing. **Jean-Louis Scartezzini:** Writing – review & editing, Funding acquisition.

Declaration of competing interest

The authors declare that they have no known competing financial interests or personal relationships that could have appeared to influence the work reported in this paper.

Acknowledgments

This research work was supported by the joint programming initiative 'ERA-Net Smart Energy Systems' focus initiative on Integrated, Regional Energy Systems, with support from the European Union's Horizon 2020 research and innovation programme [775970], and the SAFE project as part of the BRIDGE programme by the Swiss Innovation Agency (Innosuisse) [187149].

The authors acknowledge the Department of Meteorology (MISU), Stockholm University, for sharing MISU weather station data which were used in the validation study.

Appendix A

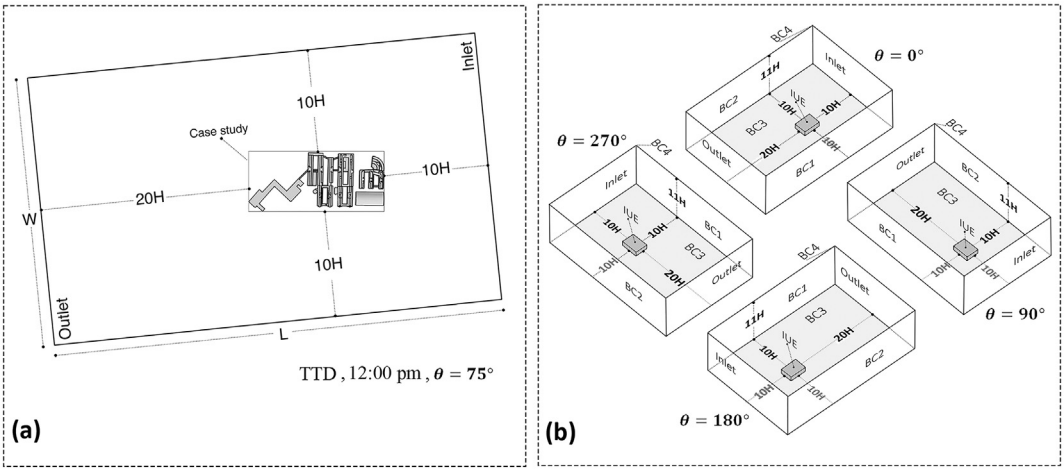

Fig. A.1. Left panel: Defined boundary conditions and computational domain for the idealized urban environments, Right panel: an example for boundary conditions and computational domain in TTD, at 12:00.

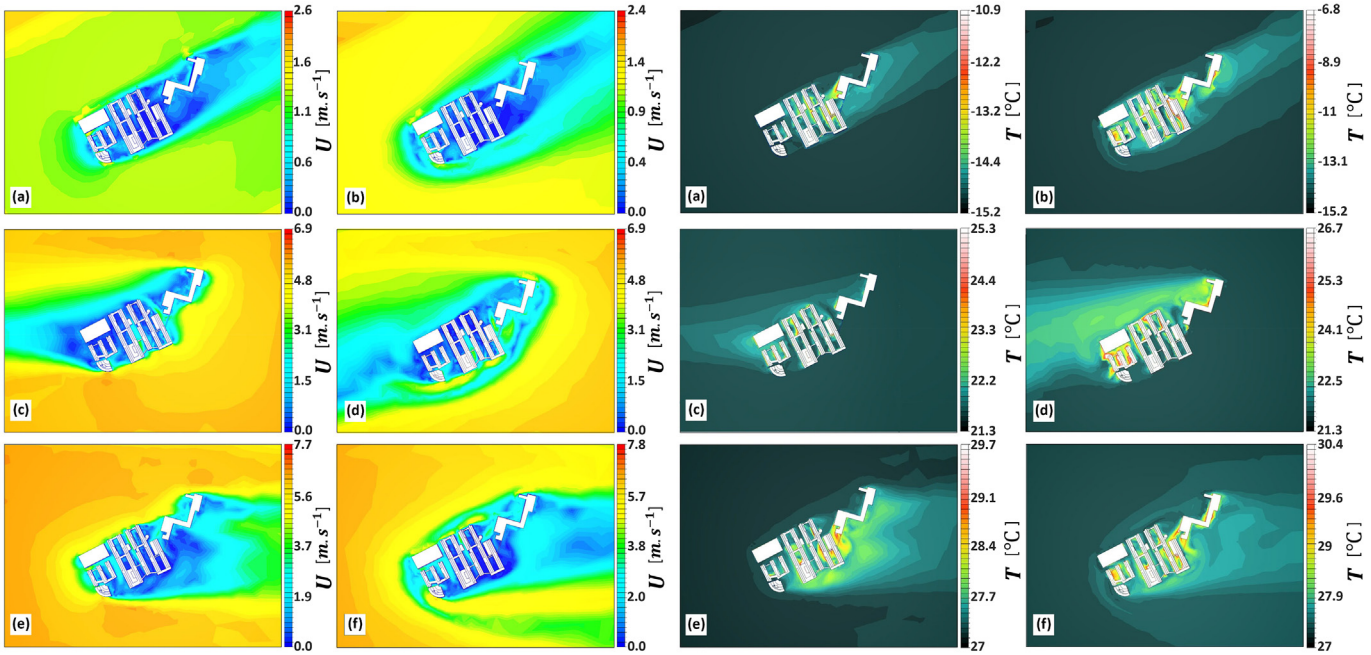

Fig. A.2. Plan-view CFD contours at 2 m above ground level for hourly wind velocity (left panel) and air temperature (right panel):ECD (Time: 3:00, WD_{ref} = 240°, U_{ref} = 2.2 m·s^{-1}, T_{ref} = −15.2 °C, RH_{ref} = 0.88): (a) Standard k-ε model, (b) AEV model.TTD (Time: 18:00, WD_{ref} = 20°, U_{ref} = 6.7 m·s^{-1}, T_{ref} = 22.3 °C, RH_{ref} = 0.91): (c) Standard k-ε model, (d) AEV model.EWD (Time: 11:00, WD_{ref} = 240°, U_{ref} = 7.8 m·s^{-1}, T_{ref} = 27 °C, RH_{ref} = 0.79): (e) Standard k-ε model, (f) AEV model.

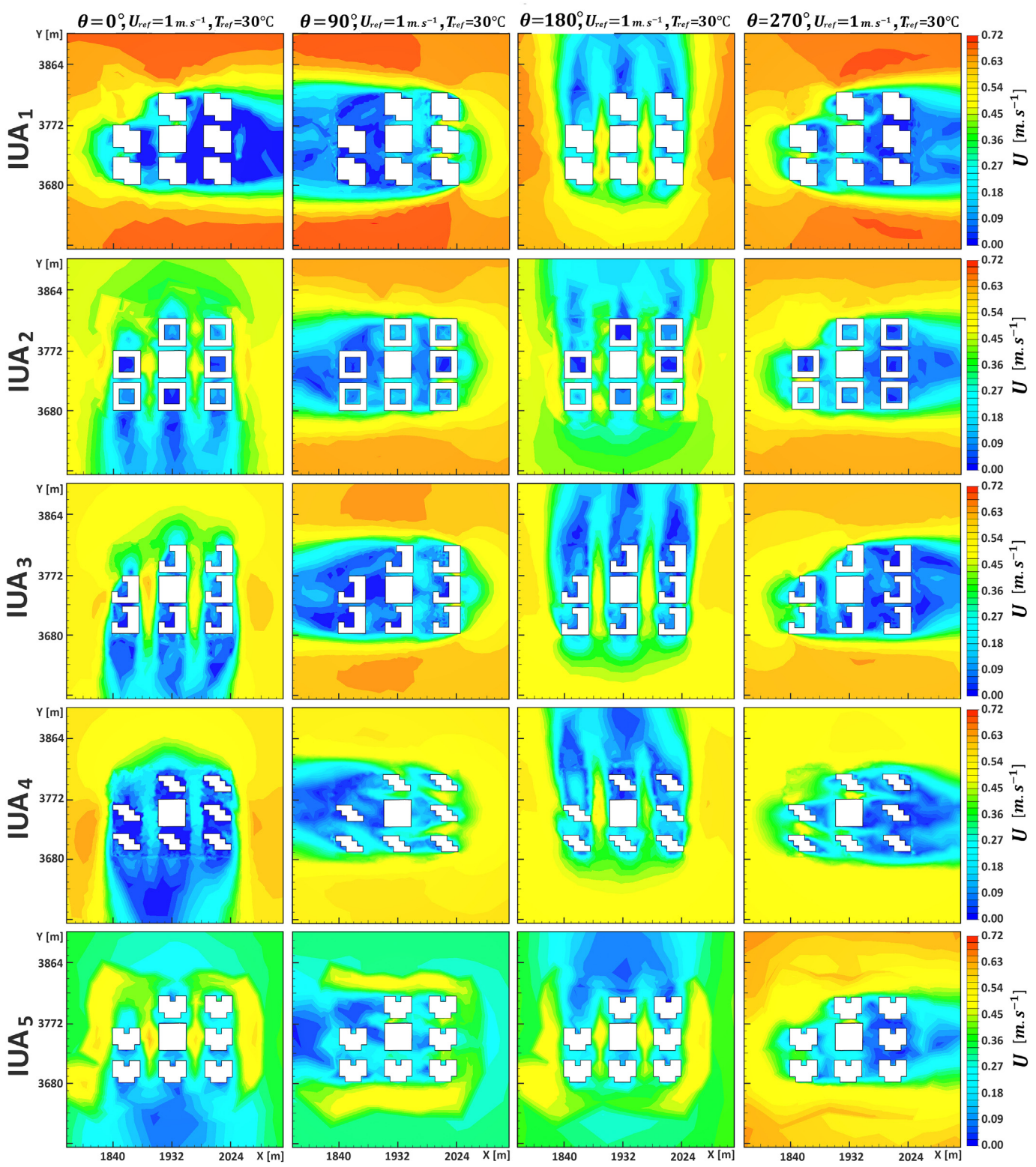

Fig. A.3. Wind speed plan-view CFD contours at 2 m above ground level.

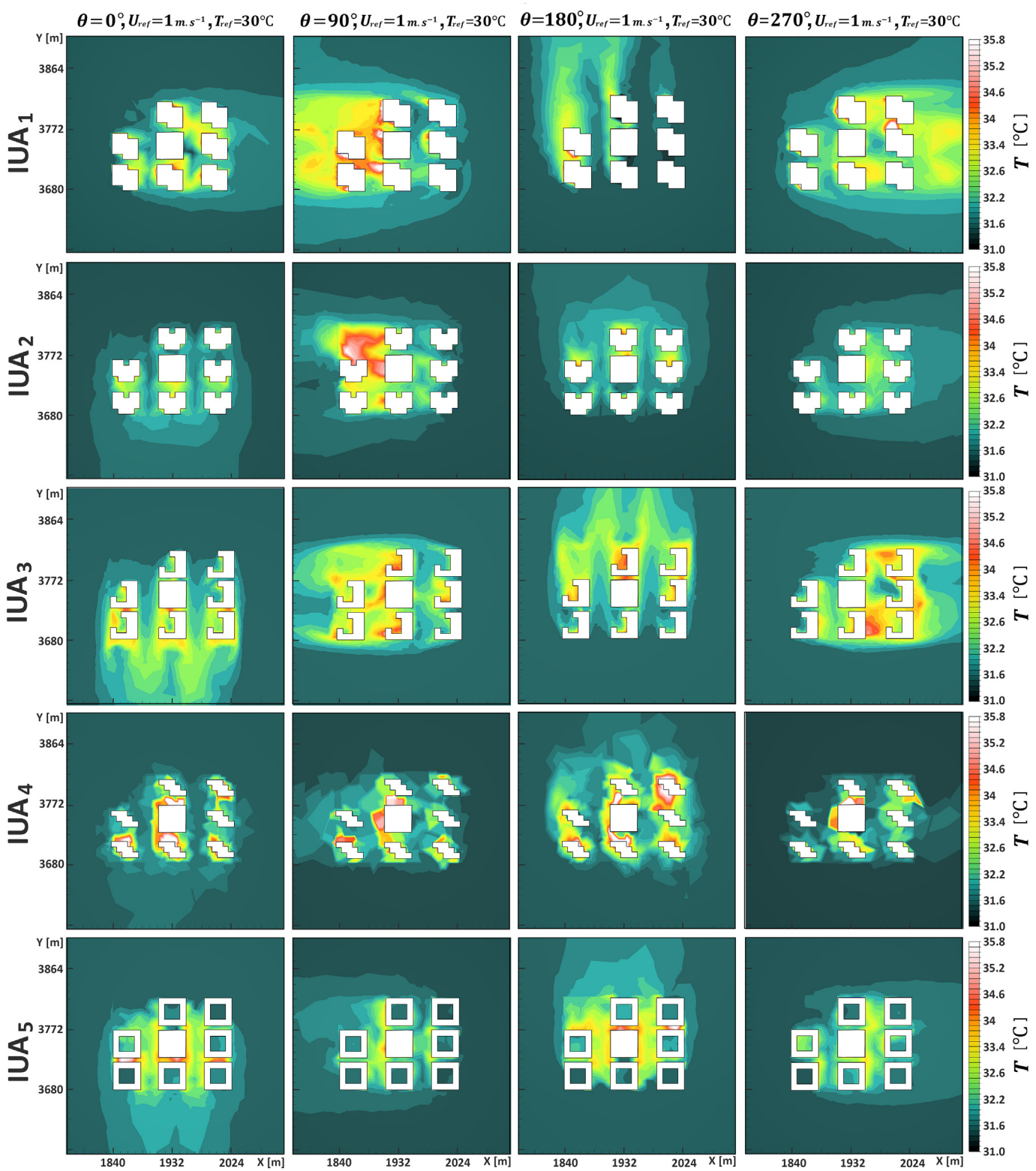

Fig. A.4. Air temperature plan-view CFD contours at 2 m above ground level.

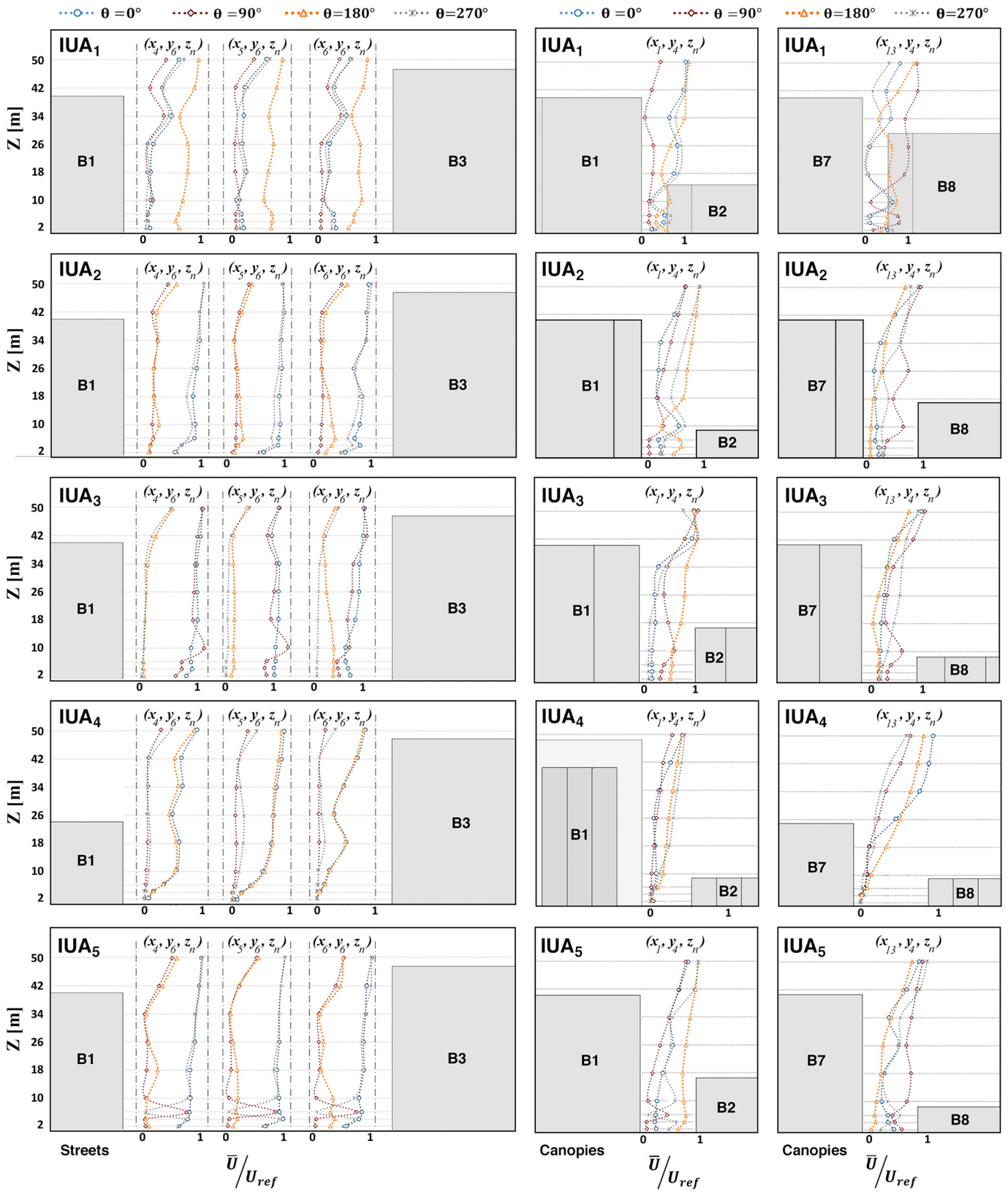

Fig. A.5. Normalized mean wind profiles in three calculation sets located in the wider streets ($x_{4,5,6}$, y_6, z_n) and two canopies including C_2 (x_1, y_4, z_n) and C_6 (x_{13}, y_4, z_n) with $U_{ref} = 5\ m{\cdot}s^{-1}$, and $T_{ref} = -15\ ^{\circ}C$.

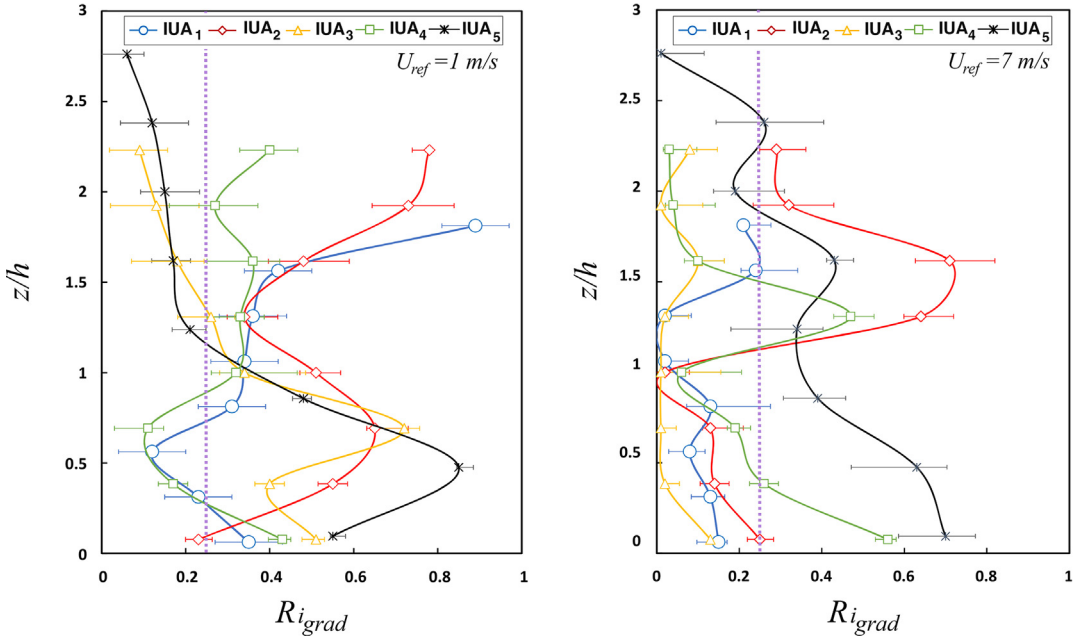

Fig. A.6. Gradient Richardson number (Ri_{grad}) as a function of height over UCL in all IUAs: Left panel: reference wind speed of 1 $m{\cdot}s^{-1}$, Right panel: reference wind speed of 7 $m{\cdot}s^{-1}$. Error bars showing the variation of climate variables based on four wind directions (θ = 0, 90, 180, 270°).

References

Abbasabadi, N., Ashayeri, M., 2019. Urban energy use modeling methods and tools: a review and an outlook. Build. Environ. 161, 106270. https://doi.org/10.1016/j.buildenv.2019.106270.

Abd Razak, A., Hagishima, A., Ikegaya, N., Tanimoto, J., 2013. Analysis of airflow over building arrays for assessment of urban wind environment. Build. Environ. 59, 56–65. https://doi.org/10.1016/j.buildenv.2012.08.007.

Achieng, K.O., 2019. Modelling of soil moisture retention curve using machine learning techniques: artificial and deep neural networks vs support vector regression models. Comput. Geosci. 133, 104320. https://doi.org/10.1016/j.cageo.2019.104320.

Alkhayat, G., Mehmood, R., 2021. A review and taxonomy of wind and solar energy forecasting methods based on deep learning. Energy AI 4, 100060. https://doi.org/10.1016/j.egyai.2021.100060.

Allegrini, J., 2018. A wind tunnel study on three-dimensional buoyant flows in street canyons with different roof shapes and building lengths. Build. Environ. 143, 71–88. https://doi.org/10.1016/j.buildenv.2018.06.056.

Allegrini, J., Dorer, V., Carmeliet, J., 2014. Buoyant flows in street canyons: validation of CFD simulations with wind tunnel measurements. Build. Environ. 72, 63–74. https://doi.org/10.1016/j.buildenv.2013.10.021.

Apreda, C., Reder, A., Mercogliano, P., 2020. Urban morphology parameterization for assessing the effects of housing blocks layouts on air temperature in the Euro-Mediterranean context. Energy Build. 223, 110171. https://doi.org/10.1016/j.enbuild.2020.110171.

Arkon, C.A., Özkol, Ü., 2014. Effect of urban geometry on pedestrian-level wind velocity. Archit. Sci. Rev. 57, 4–19. https://doi.org/10.1080/00038628.2013.835709.

Asadi, A., Arefi, H., Fathipoor, H., 2020. Simulation of green roofs and their potential mitigating effects on the urban heat island using an artificial neural network: a case study in Austin, Texas. Adv. Space Res. 66, 1846–1862. https://doi.org/10.1016/j.asr.2020.06.039.

Aslam, S., Herodotou, H., Mohsin, S.M., Javaid, N., Ashraf, N., Aslam, S., 2021. A survey on deep learning methods for power load and renewable energy forecasting in smart microgrids. Renew. Sust. Energ. Rev. 144, 110992. https://doi.org/10.1016/j.rser.2021.110992.

Basheer, I.A., Hajmeer, M., 2000. Artificial neural networks: fundamentals, computing, design, and application. J. Microbiol. Methods 43, 3–31. https://doi.org/10.1016/S0167-7012(00)00201-3.

Bazargan, M., Mohseni, M., 2012. Algebraic zero-equation versus complex two-equation turbulence modeling in supercritical fluid flows. Comput. Fluids 60, 49–57. https://doi.org/10.1016/j.compfluid.2012.02.022.

Beck, H.E., Zimmermann, N.E., McVicar, T.R., Vergopolan, N., Berg, A., Wood, E.F., 2018. Present and future Köppen-Geiger climate classification maps at 1-km resolution. Sci. Data 5, 1–12. https://doi.org/10.1038/sdata.2018.214.

Becker, R., Thrän, D., 2017. Completion of wind turbine data sets for wind integration studies applying random forests and k-nearest neighbors. Appl. Energy 208, 252–262. https://doi.org/10.1016/j.apenergy.2017.10.044.

Bhatta, B., 2010. Causes and consequences of urban growth and sprawl. In: Bhatta, B. (Ed.), Analysis of Urban Growth and Sprawl From Remote Sensing Data. Springer, Berlin, Heidelberg, pp. 17–36 https://doi.org/10.1007/978-3-642-05299-6_2.

Blocken, B., 2015. Computational fluid dynamics for urban physics: importance, scales, possibilities, limitations and ten tips and tricks towards accurate and reliable simulations. Build. Environ. 91, 219–245. https://doi.org/10.1016/j.buildenv.2015.02.015.

Brockerhoff, M., Nations U, 2018. World urbanization prospects: the 2018 revision. Popul. Dev. Rev. 24, 883. https://doi.org/10.2307/2808041.

Cao, Q., Luan, Q., Liu, Y., Wang, R., 2021. The effects of 2D and 3D building morphology on urban environments: a multi-scale analysis in the Beijing metropolitan region. Build. Environ., 107635 https://doi.org/10.1016/j.buildenv.2021.107635.

Castaldo, V.L., Pisello, A.L., Piselli, C., Fabiani, C., Cotana, F., Santamouris, M., 2018. How outdoor microclimate mitigation affects building thermal-energy performance: a new design-stage method for energy saving in residential near-zero energy settlements in Italy. Renew. Energy 127, 920–935. https://doi.org/10.1016/j.renene.2018.04.090.

CFD 2019 Documentation | Autodesk Knowledge Network n.d. https://knowledge.autodesk.com/support/cfd/learn-explore/caas/CloudHelp/cloudhelp/2019/ENU/SimCFD-Learning/files/GUID-DEE0664D-771B-4446-9ED4-1498267D13FB-htm.html (accessed April 7, 2021).

Chen, Y., Wu, J., Yu, K., Wang, D., 2020. Evaluating the impact of the building density and height on the block surface temperature. Build. Environ. 168, 106493. https://doi.org/10.1016/j.buildenv.2019.106493.

Chokhachian, A., Perini, K., Giulini, S., Auer, T., 2020. Urban performance and density: generative study on interdependencies of urban form and environmental measures. Sustain. Cities Soc. 53, 101952. https://doi.org/10.1016/j.scs.2019.101952.

City Planning Administration, 2018. Stockholm City Plan. Stockholm Municipality.

Dirksen, M., Ronda, R.J., Theeuwes, N.E., Pagani, G.A., 2019. Sky view factor calculations and its application in urban heat island studies. Urban Clim. 30, 100498. https://doi.org/10.1016/j.uclim.2019.100498.

Ferrero Bermejo, J., Gómez Fernández, J.F., Olivencia Polo, F., Crespo Márquez, A., 2019. A review of the use of artificial neural network models for energy and reliability prediction. A study of the solar PV, hydraulic and wind energy sources. Appl. Sci. 9, 1844. https://doi.org/10.3390/app9091844.

Garuma, G.F., 2018. Review of urban surface parameterizations for numerical climate models. Urban Clim. 24, 830–851. https://doi.org/10.1016/j.uclim.2017.10.006.

Giometto, M.G., Christen, A., Meneveau, C., Fang, J., Krafczyk, M., Parlange, M.B., 2016. Spatial characteristics of roughness sublayer mean flow and turbulence over a realistic urban surface. Bound.-Layer Meteorol. 160, 425–452. https://doi.org/10.1007/s10546-016-0157-6.

Giridharan, R., Emmanuel, R., 2018. The impact of urban compactness, comfort strategies and energy consumption on tropical urban heat island intensity: a review. Sustain. Cities Soc. 40, 677–687. https://doi.org/10.1016/j.scs.2018.01.024.

Guillén-Lambea, S., Rodríguez-Soria, B., Marín, J.M., 2019. Air infiltrations and energy demand for residential low energy buildings in warm climates. Renew. Sust. Energ. Rev. 116, 109469. https://doi.org/10.1016/j.rser.2019.109469.

Han, J.M., Ang, Y.Q., Malkawi, A., Samuelson, H.W., 2021. Using recurrent neural networks for localized weather prediction with combined use of public airport data and on-site measurements. Build. Environ. 192, 107601. https://doi.org/10.1016/j.buildenv.2021.107601.

Hochreiter, S., Schmidhuber, J., 1997. Long short-term memory. Neural Comput. 9, 1735–1780. https://doi.org/10.1162/neco.1997.9.8.1735.

Hosseini, M., Javanroodi, K., Nik, V.M., 2022. High-resolution impact assessment of climate change on building energy performance considering extreme weather events and microclimate – investigating variations in indoor thermal comfort and degree-days. Sustain. Cities Soc. 78, 103634. https://doi.org/10.1016/j.scs.2021.103634.
Hsieh, C.-M., Huang, H.-C., 2016. Mitigating urban heat islands: a method to identify potential wind corridor for cooling and ventilation. Comput. Environ. Urban. Syst. 57, 130–143. https://doi.org/10.1016/j.compenvurbsys.2016.02.005.
Hu, Q., Zhang, R., Zhou, Y., 2016. Transfer learning for short-term wind speed prediction with deep neural networks. Renew. Energy 85, 83–95. https://doi.org/10.1016/j.renene.2015.06.034.
IVA, 2017. Drivers and Consequences of Urban Development. IVA. https://www.iva.se/globalassets/rapporter/framtidens-goda-stad/201705-iva-framtidensgodastad-delrapport-urbanisering-english-c.pdf.
Jamei, E., Ossen, D.R., Rajagopalan, P., 2017. Investigating the effect of urban configurations on the variation of air temperature. Int. J. Sustain. Built Environ. 6, 389–399. https://doi.org/10.1016/j.ijsbe.2017.07.001.
Javanroodi, K., Nik, V.M., 2019. Impacts of microclimate conditions on the energy performance of buildings in urban areas. Buildings, 9 https://doi.org/10.3390/buildings9080189.
Javanroodi, K., Nik, V.M., 2020. Interactions between extreme climate and urban morphology: investigating the evolution of extreme wind speeds from mesoscale to microscale. Urban Clim. 31, 100544. https://doi.org/10.1016/j.uclim.2019.100544.
Javanroodi, K., Mahdavinejad, M., Nik, V.M., 2018. Impacts of urban morphology on reducing cooling load and increasing ventilation potential in hot-arid climate. Appl. Energy 231, 714–746. https://doi.org/10.1016/j.apenergy.2018.09.116.
Javanroodi, K., Nik, V.M., Mahdavinejad, M., 2019. A novel design-based optimization framework for enhancing the energy efficiency of high-rise office buildings in urban areas. Sustain. Cities Soc. 49, 101597. https://doi.org/10.1016/j.scs.2019.101597.
Javanroodi, K., Nik, V.M., Scartezzini, J., 2021. Quantifying the impacts of urban morphology on modifying microclimate conditions in extreme weather conditions. J. Phys. Conf. Ser. 2042, 012058. https://doi.org/10.1088/1742-6596/2042/1/012058.
Kalogirou, S.A., 2001. Artificial neural networks in renewable energy systems applications: a review. Renew. Sust. Energ. Rev. 5, 373–401. https://doi.org/10.1016/S1364-0321(01)00006-5.
Kikumoto, H., Ooka, R., Han, M., Nakajima, K., 2018. Consistency of mean wind speed in pedestrian wind environment analyses: mathematical consideration and a case study using large-eddy simulation. J. Wind Eng. Ind. Aerodyn. 173, 91–99. https://doi.org/10.1016/j.jweia.2017.11.021.
Kono, T., Tamura, T., Ashie, Y., 2010. Numerical investigations of mean winds within canopies of regularly arrayed cubical buildings under neutral stability conditions. Bound.-Layer Meteorol. 134, 131–155. https://doi.org/10.1007/s10546-009-9434-y.
Lenz, S., Schönherr, M., Geier, M., Krafczyk, M., Pasquali, A., Christen, A., et al., 2019. Towards real-time simulation of turbulent air flow over a resolved urban canopy using the cumulant lattice Boltzmann method on a GPGPU. J. Wind Eng. Ind. Aerodyn. 189, 151–162. https://doi.org/10.1016/j.jweia.2019.03.012.
Li, X., Zhou, Y., Yu, S., Jia, G., Li, H., Li, W., 2019. Urban heat island impacts on building energy consumption: a review of approaches and findings. Energy 174, 407–419. https://doi.org/10.1016/j.energy.2019.02.183.
Lin, L., Luo, M., Chan, T.O., Ge, E., Liu, X., Zhao, Y., et al., 2019. Effects of urbanization on winter wind chill conditions over China. Sci. Total Environ. 688, 389–397. https://doi.org/10.1016/j.scitotenv.2019.06.145.
Lin, L., Gao, T., Luo, M., Ge, E., Yang, Y., Liu, Z., et al., 2020. Contribution of urbanization to the changes in extreme climate events in urban agglomerations across China. Sci. Total Environ. 744, 140264. https://doi.org/10.1016/j.scitotenv.2020.140264.
Lin, Y., Ichinose, T., Yamao, Y., Mouri, H., 2020. Wind velocity and temperature fields under different surface heating conditions in a street canyon in wind tunnel experiments. Build. Environ. 168, 106500. https://doi.org/10.1016/j.buildenv.2019.106500.
Liu, L., Liu, J., Jin, L., Liu, L., Gao, Y., Pan, X., 2020. Climate-conscious spatial morphology optimization strategy using a method combining local climate zone parameterization concept and urban canopy layer model. Build. Environ. 185, 107301. https://doi.org/10.1016/j.buildenv.2020.107301.
Liu, M.-D., Ding, L., Bai, Y.-L., 2021. Application of hybrid model based on empirical mode decomposition, novel recurrent neural networks and the ARIMA to wind speed prediction. Energy Convers. Manag. 233, 113917. https://doi.org/10.1016/j.enconman.2021.113917.
Liu, X., Zhou, J., Qian, H., 2021. Short-term wind power forecasting by stacked recurrent neural networks with parametric sine activation function. Electr. Power Syst. Res. 192, 107011. https://doi.org/10.1016/j.epsr.2020.107011.
Localities and Urban Areas 2018. Statistics Sweden.
Mandal, B.C., Mazumdar, H.P., 2015. The importance of the law of the wall. Int. J. Appl. Mech. Eng. 20, 857–869. https://doi.org/10.1515/ijame-2015-0055.
Marquez, R., Pedro, H.T.C., Coimbra, C.F.M., 2013. Hybrid solar forecasting method uses satellite imaging and ground telemetry as inputs to ANNs. Sol. Energy 92, 176–188. https://doi.org/10.1016/j.solener.2013.02.023.
Marugán, A.P., Márquez, F.P.G., Perez, J.M.P., Ruiz-Hernández, D., 2018. A survey of artificial neural network in wind energy systems. Appl. Energy 228, 1822–1836. https://doi.org/10.1016/j.apenergy.2018.07.084.
Mauree, D., Castello, R., Mancini, G., Nutta, T., Zhang, T., Scartezzini, J.-L., 2019. Wind profile prediction in an urban canyon: a machine learning approach. J. Phys. Conf. Ser. 1343, 012047. https://doi.org/10.1088/1742-6596/1343/1/012047.
Mba, L., Meukam, P., Kemajou, A., 2016. Application of artificial neural network for predicting hourly indoor air temperature and relative humidity in modern building in humid region. Energy Build. 121, 32–42. https://doi.org/10.1016/j.enbuild.2016.03.046.
Mi, X., Zhao, S., 2020. Wind speed prediction based on singular spectrum analysis and neural network structural learning. Energy Convers. Manag. 216, 112956. https://doi.org/10.1016/j.enconman.2020.112956.
Mittal, H., Sharma, A., Gairola, A., 2018. A review on the study of urban wind at the pedestrian level around buildings. J. Build. Eng. 18, 154–163. https://doi.org/10.1016/j.jobe.2018.03.006.
Mo, Z., Liu, C.-H., Ho, Y.-K., 2021. Roughness sublayer flows over real urban morphology: a wind tunnel study. Build. Environ. 188, 107463. https://doi.org/10.1016/j.buildenv.2020.107463.
Mocanu, D.C., Mocanu, E., Stone, P., Nguyen, P.H., Gibescu, M., Liotta, A., 2018. Scalable training of artificial neural networks with adaptive sparse connectivity inspired by network science. Nat. Commun. 9, 2383. https://doi.org/10.1038/s41467-018-04316-3.
Mochida, A., Tominaga, Y., Murakami, S., Yoshie, R., Ishihara, T., Ooka, R., 2002. Comparison of various k-ε models and DSM applied to flow around a high-rise building - report on AIJ cooperative project for CFD prediction of wind environment -. Wind Struct. 5, 227–244. https://doi.org/10.12989/was.2002.5.2_3_4.227.
Mohandes, S.R., Zhang, X., Mahdiyar, A., 2019. A comprehensive review on the application of artificial neural networks in building energy analysis. Neurocomputing 340, 55–75. https://doi.org/10.1016/j.neucom.2019.02.040.
Moonen, P., Defraeye, T., Dorer, V., Blocken, B., Carmeliet, J., 2012. Urban physics: effect of the micro-climate on comfort, health and energy demand. Front. Archit. Res. 1, 197–228. https://doi.org/10.1016/j.foar.2012.05.002.
Mortezazadeh, M., Jandaghian, Z., Wang, L.L., 2021. Integrating CityFFD and WRF for modeling urban microclimate under heatwaves. Sustain. Cities Soc. 66, 102670. https://doi.org/10.1016/j.scs.2020.102670.
Nardecchia, F., Gugliermetti, F., Bisegna, F., 2016. How temperature affects the airflow around a single-block isolated building. Energy Build. 118, 142–151. https://doi.org/10.1016/j.enbuild.2016.03.003.
Nielsen, M.M., 2015. Remote sensing for urban planning and management: the use of window-independent context segmentation to extract urban features in Stockholm. Comput. Environ. Urban. Syst. 52, 1–9. https://doi.org/10.1016/j.compenvurbsys.2015.02.002.
Nik, V.M., 2016. Making energy simulation easier for future climate – synthesizing typical and extreme weather data sets out of regional climate models (RCMs). Appl. Energy 177, 204–226. https://doi.org/10.1016/j.apenergy.2016.05.107.
Oke, T.R., 1987. Boundary Layer Climates. Routledge.
Oke, T.R., 2017. Urban Climates. 1st edition. Cambridge University Press, Cambridge.
Panchal, G., Ganatra, A., Kosta, Y.P., Panchal, D., 2011. Behaviour analysis of multilayer perceptronswith multiple hidden neurons and hidden layers. IJCTE, 332–337 https://doi.org/10.7763/IJCTE.2011.V3.328.
Papantoniou, S., Kolokotsa, D.-D., 2016. Prediction of outdoor air temperature using neural networks: application in 4 European cities. Energy Build. 114, 72–79. https://doi.org/10.1016/j.enbuild.2015.06.054.
Patankar, S., 1980. Numerical Heat Transfer and Fluid Flow. 1st edition. CRC Press, New York.
Peng, Y., Feng, T., Timmermans, H., 2019. A path analysis of outdoor comfort in urban public spaces. Build. Environ. 148, 459–467. https://doi.org/10.1016/j.buildenv.2018.11.023.
Perera, A.T.D., Javanroodi, K., Nik, V.M., 2021. Climate resilient interconnected infrastructure: co-optimization of energy systems and urban morphology. Appl. Energy, 285 https://doi.org/10.1016/j.apenergy.2020.116430.
Perera, A.T.D., Javanroodi, K., Wang, Y., Hong, T., 2021. Urban cells: extending the energy hub concept to facilitate sector and spatial coupling. Adv. Appl. Energy 3, 100046. https://doi.org/10.1016/J.ADAPEN.2021.100046.
Ricci, A., Kalkman, I., Blocken, B., Burlando, M., Repetto, M.P., 2020. Impact of turbulence models and roughness height in 3D steady RANS simulations of wind flow in an urban environment. Build. Environ. 171, 106617. https://doi.org/10.1016/j.buildenv.2019.106617.
Richards, P.J., Hoxey, R.P., Short, L.J., 2001. Wind pressures on a 6m cube. J. Wind Eng. Ind. Aerodyn. 89, 1553–1564. https://doi.org/10.1016/S0167-6105(01)00139-8.
Roman, N.D., Bre, F., Fachinotti, V.D., Lamberts, R., 2020. Application and characterization of metamodels based on artificial neural networks for building performance simulation: a systematic review. Energy Build. 217, 109972. https://doi.org/10.1016/j.enbuild.2020.109972.
Rynkiewicz, J., 2012. General bound of overfitting for MLP regression models. Neurocomputing 90, 106–110. https://doi.org/10.1016/j.neucom.2011.11.028.
Schinasi, L.H., Benmarhnia, T., De Roos, A.J., 2018. Modification of the association between high ambient temperature and health by urban microclimate indicators: a systematic review and meta-analysis. Environ. Res. 161, 168–180. https://doi.org/10.1016/j.envres.2017.11.004.
Schnipke, R., 1986. A Streamline Upwind Finite Element Method for Laminar and Turbulent Flow.
Sousa, J., Gorlé, C., 2019. Computational urban flow predictions with Bayesian inference: validation with field data. Build. Environ. 154, 13–22. https://doi.org/10.1016/j.buildenv.2019.02.028.
Su, Q., Liao, X., Carin, L., 2017. A Probabilistic Framework for Nonlinearities in Stochastic Neural Networks. ArXiv:170906123 [Cs, Stat].
Sweden Weather|SMHI n.d. https://www.smhi.se/en/weather (accessed February 13, 2020).
Sweden's National Report for the third United Nations Conference on Housing and Sustainable Urban Development (Habitat III). Swedish National Report; n.d.
Taleghani, M., Marshall, A., Fitton, R., Swan, W., 2019. Renaturing a microclimate: the impact of greening a neighbourhood on indoor thermal comfort during a heatwave in Manchester, UK. Solar Energy 182, 245–255. https://doi.org/10.1016/j.solener.2019.02.062.
TensorFlow White Papers, TensorFlow. https://www.tensorflow.org/about/bib (accessed February 2, 2021).
Toja-Silva, F., Kono, T., Peralta, C., Lopez-Garcia, O., Chen, J., 2018. A review of computational fluid dynamics (CFD) simulations of the wind flow around buildings for urban wind energy exploitation. J. Wind Eng. Ind. Aerodyn. 180, 66–87. https://doi.org/10.1016/j.jweia.2018.07.010.

Tominaga, Y., Mochida, A., Yoshie, R., Kataoka, H., Nozu, T., Yoshikawa, M., et al., 2008. AIJ guidelines for practical applications of CFD to pedestrian wind environment around buildings. J. Wind Eng. Ind. Aerodyn. 96, 1749–1761. https://doi.org/10.1016/j.jweia.2008.02.058.

Toparlar, Y., Blocken, B., Maiheu, B., van Heijst, G.J.F., 2017. A review on the CFD analysis of urban microclimate. Renew. Sust. Energ. Rev. 80, 1613–1640. https://doi.org/10.1016/j.rser.2017.05.248.

Tsichritzis, L., Nikolopoulou, M., 2019. The effect of building height and façade area ratio on pedestrian wind comfort of London. J. Wind Eng. Ind. Aerodyn. 191, 63–75. https://doi.org/10.1016/j.jweia.2019.05.021.

Varoquaux, G., Buitinck, L., Louppe, G., Grisel, O., Pedregosa, F., Mueller, A., 2015. Scikit-learn: Machine Learning Without Learning the Machinery. GetMobile: Mobile Comp and Comm. 19, pp. 29–33. https://doi.org/10.1145/2786984.2786995.

Wang, Y., Wu, L., 2016. On practical challenges of decomposition-based hybrid forecasting algorithms for wind speed and solar irradiation. Energy 112, 208–220. https://doi.org/10.1016/j.energy.2016.06.075.

Wang, J., Song, Y., Liu, F., Hou, R., 2016. Analysis and application of forecasting models in wind power integration: a review of multi-step-ahead wind speed forecasting models. Renew. Sust. Energ. Rev. 60, 960–981. https://doi.org/10.1016/j.rser.2016.01.114.

Wang, J., Zhang, T., Wang, S., Battaglia, F., 2018. Numerical investigation of single-sided natural ventilation driven by buoyancy and wind through variable window configurations. Energy Build. 168, 147–164. https://doi.org/10.1016/j.enbuild.2018.03.015.

Weather Station - Department of meteorology n.d. https://www.misu.su.se/research/weather-station (accessed January 14, 2020).

World Urbanization Prospects, 2018. Population Division - United Nations-2014 Revision. NewYork.

Xu, Y., Ren, C., Ma, P., Ho, J., Wang, W., Lau, K.K.-L., et al., 2017. Urban morphology detection and computation for urban climate research. Landsc. Urban Plan. 167, 212–224. https://doi.org/10.1016/j.landurbplan.2017.06.018.

Yang, J., Shi, B., Shi, Y., Marvin, S., Zheng, Y., Xia, G., 2020. Air pollution dispersal in high density urban areas: research on the triadic relation of wind, air pollution, and urban form. Sustain. Cities Soc. 54, 101941. https://doi.org/10.1016/j.scs.2019.101941.

Yang, Y., Javanroodi, K., Nik, V.M., 2021. Climate change and energy performance of European residential building stocks – a comprehensive impact assessment using climate big data from the coordinated regional climate downscaling experiment. Appl. Energy 298, 117246. https://doi.org/10.1016/j.apenergy.2021.117246.

Yang, Y., Javanroodi, K., Nik, V.M., 2022. Climate change and renewable energy generation in Europe—long-term impact assessment on solar and wind energy using high-resolution future climate data and considering climate uncertainties. Energies 15, 302. https://doi.org/10.3390/en15010302.

Yi, Y.K., Kim, H., 2017. Universal visible sky factor: a method for calculating the three-dimensional visible sky ratio. Build. Environ. 123, 390–403. https://doi.org/10.1016/j.buildenv.2017.06.044.

Yi, Y.K., Malkawi, A.M., 2011. Integrating neural network models with computational fluid dynamics (CFD) for site-specific wind condition. Build. Simul. 4, 245. https://doi.org/10.1007/s12273-011-0042-7.

Yuan, C., Adelia, A.S., Mei, S., He, W., Li, X.-X., Norford, L., 2020. Mitigating intensity of urban heat island by better understanding on urban morphology and anthropogenic heat dispersion. Build. Environ. 176, 106876. https://doi.org/10.1016/j.buildenv.2020.106876.

Yuan, Q., Shen, H., Li, T., Li, Z., Li, S., Jiang, Y., et al., 2020. Deep learning in environmental remote sensing: achievements and challenges. Remote Sens. Environ. 241, 111716. https://doi.org/10.1016/j.rse.2020.111716.

Zendehboudi, A., Baseer, M.A., Saidur, R., 2018. Application of support vector machine models for forecasting solar and wind energy resources: a review. J. Clean. Prod. 199, 272–285. https://doi.org/10.1016/j.jclepro.2018.07.164.

Zhang, X., Tse, K.T., Weerasuriya, A.U., Li, S.W., Kwok, K.C.S., Mak, C.M., et al., 2017. Evaluation of pedestrian wind comfort near 'lift-up' buildings with different aspect ratios and central core modifications. Build. Environ. 124, 245–257. https://doi.org/10.1016/j.buildenv.2017.08.012.

Zhang, J., Xu, L., Shabunko, V., Tay, S.E.R., Sun, H., Lau, S.S.Y., et al., 2019. Impact of urban block typology on building solar potential and energy use efficiency in tropical high-density city. Appl. Energy 240, 513–533. https://doi.org/10.1016/j.apenergy.2019.02.033.

Zhou, M., Wang, B., Guo, S., Watada, J., 2021. Multi-objective prediction intervals for wind power forecast based on deep neural networks. Inf. Sci. 550, 207–220. https://doi.org/10.1016/j.ins.2020.10.034.